

REPORT DOCUMENTATION PAGE		Form Approved OMB No. 0704-0188
Public reporting burden for this collection of information is estimated to average 1 hour per response, including the time for reviewing instructions, searching existing data sources, gathering and maintaining the data needed, and completing and reviewing this collection of information. Send comments regarding this burden estimate or any other aspect of this collection of information, including suggestions for reducing this burden to Department of Defense, Washington Headquarters Services, Directorate for Information Operations and Reports (0704-0188), 1215 Jefferson Davis Highway, Suite 1204, Arlington, VA 22202-4302. Respondents should be aware that notwithstanding any other provision of law, no person shall be subject to any penalty for failing to comply with a collection of information if it does not display a currently valid OMB control number. PLEASE DO NOT RETURN YOUR FORM TO THE ABOVE ADDRESS.		
1. REPORT DATE (DD-MM-YYYY) 12/12/2006	2. REPORT TYPE FINAL PERFORMANCE REPORT	3. DATES COVERED (From - To) 4/01/2003-9/30/2006
4. TITLE AND SUBTITLE  FATIGUE AND FRACTURE OF POLYCRYSTALLINE SILICON AND DIAMOND MEMS AT ROOM AND ELEVATED TEMPERATURES		5a. CONTRACT NUMBER
		5b. GRANT NUMBER F49620-03-1-0080
		5c. PROGRAM ELEMENT NUMBER
6. AUTHOR(S)  IOANNIS CHASIOTIS  Aerospace Engineering, U. Illinois at Urbana-Champaign, M/C 236 305A Talbot Lab, 104 South Wright St., Urbana, IL 61801		5d. PROJECT NUMBER
		5e. TASK NUMBER
		5f. WORK UNIT NUMBER
7. PERFORMING ORGANIZATION NAME(S) AND ADDRESS(ES)  UNIVERSITY OF VIRGINIA 122 Engineer's Way PO BOX 400746 Charlottesville, VA 22904		8. PERFORMING ORGANIZATION REPORT
9. SPONSORING / MONITORING AGENCY NAME(S) AND ADDRESS(ES)  Air Force Office of Scientific Research (AFOSR) Program: Mechanics of Multifunctional Materials and Microsystems <i>Dr. Byung Up Lee / NA</i>		10. SPONSOR/MONITOR'S ACRONYM(S) Program Manager: Dr. B.L. Lee
		11. SPONSOR/MONITOR'S REPORT NUMBER(S)
12. DISTRIBUTION / AVAILABILITY STATEMENT  Approved for public release, Distribution unlimited		
13. SUPPLEMENTARY NOTES		
14. ABSTRACT A high-resolution Atomic Force Microscopy (AFM)/Digital Image Correlation (DIC) method was developed to investigate the deformation and fracture of tetrahedral amorphous diamond-like carbon (ta-C) and polycrystalline silicon (polysilicon) for microelectromechanical systems (MEMS). Polysilicon and ta-C test structures were fabricated at the Sandia National Laboratories (SNL) and at MCNC-Cronos. Their Young's modulus, Poisson's ratio, strength, and fracture toughness were obtained, many of them for the first time. Compared to polysilicon, ta-C was found to have superior mechanical properties: Its fracture toughness and strength were 3.5 times and two times that of polysilicon, respectively. Its elastic modulus was 4.5 times that of polysilicon and its Poisson's ratio was 30% smaller than polysilicon. The mode I and mixed mode I/II fracture toughness of polysilicon showed 50% scatter due to its polycrystallinity. On the contrary, the mixed mode I/II fracture of the amorphous ta-C was described well by deterministic theories for brittle fracture. The stochastic failure of polysilicon was treated by a finite element model that combined NASA's code CARES Life (Ceramics Analysis and Reliability Evaluation of Structures Life). This model provided failure predictions for devices with arbitrary geometries. Finally, the multi-grain nature of polysilicon was found to present a potential risk in the accurate determination of its effective mechanical behavior, especially in MEMS with dimensions equal to a small multiple of the grain size. In general, devices with dimensions larger than 15x15 grains can be described by using the isotropic properties reported in literature and presented in this report.		

AFRL-SR-AR-TR-07-0099

<b>15. SUBJECT TERMS</b>				
<b>16. SECURITY CLASSIFICATION OF:</b>			<b>17. LIMITATION OF ABSTRACT</b>	<b>18. NUMBER OF PAGES</b>
<b>a. REPORT</b>	<b>b. ABSTRACT</b>	<b>c. THIS PAGE</b>		<b>34</b>
				<b>19a. NAME OF RESPONSIBLE PERSON</b>
				<b>19b. TELEPHONE NUMBER</b> (include area code) (217) -244-1474

Standard Form 298  
(Rev. 8-98)  
Prescribed by ANSI Std.  
Z39.18



UNIVERSITY OF ILLINOIS  
AEROSPACE ENGINEERING



# **FINAL PERFORMANCE REPORT**

**Reporting Dates: 4/01/2003-9/30/2006**

## **FATIGUE AND FRACTURE OF POLYCRYSTALLINE SILICON AND DIAMOND MEMS AT ROOM AND ELEVATED TEMPERATURES**

**PI: Ioannis Chasiotis**

Aerospace Engineering

University of Illinois at Urbana-Champaign

Talbot Lab, 104 S. Wright Street, Urbana, IL 61801

Telephone: (217) 244-1474, Fax: (217) 244-0720, E-mail: [chasioti@uiuc.edu](mailto:chasioti@uiuc.edu)

---

**AFOSR GRANT # F49620-03-1-0080**

Program Manager: Dr. B.L. Lee

# **20070323328**

DECEMBER 2006

## SUMMARY

A high-resolution experimental method was developed to investigate the deformation and fracture properties of tetrahedral amorphous diamond-like carbon (ta-C) and polycrystalline silicon (polysilicon) for microelectromechanical systems (MEMS). The method employed an Atomic Force Microscope (AFM) to record strains in micron scale tensile specimens with the aid of Digital Image Correlation (DIC). Polysilicon and ta-C test structures were fabricated at the Sandia National Laboratories (SNL) and at MCNC-Cronos and their Young's modulus, Poisson's ratio, tensile strength, and fracture toughness were obtained by the AFM/DIC method, many of them for the first time. When compared to traditionally employed polysilicon, ta-C was found to have superior mechanical properties: its fracture toughness was 3.5 times that of polysilicon and its strength was at least twice that of polysilicon. These outstanding fracture properties provide increased resistance to failure. The elastic modulus of ta-C was found to be 4.5 times that of polysilicon and its Poisson's ratio was 30% smaller than polysilicon. These elastic properties will provide enhanced dimensional stability in addition to the superb wear resistance of ta-C.

The mode I and mixed mode I/II fracture toughnesses of polysilicon were subject to 50% scatter due to its polycrystalline structure. On the contrary, the mixed mode I/II fracture of amorphous ta-C was described very well by existing deterministic theories for fracture of brittle materials. The stochastic failure of polysilicon was treated in a comprehensive finite element model that combined NASA's code CARES Life (Ceramics Analysis and Reliability Evaluation of Structures) and identification of the flaw population that is responsible for failure. This model allowed for the prediction of failure of MEMS devices with arbitrary geometries. This study pointed out to a potential pitfall in blindly using the Weibull cumulative probability density function to present strength data from microscale specimens: The active flaw population changes with the component size and its local geometry which implies that the flaw population is not always the same between self-similar device geometries. Finally, the multigrain nature of polysilicon was found experimentally to present a potential risk in the accurate determination of its effective mechanical behavior, especially when it is used to fabricate devices with dimensions on the order of a few microns, which is a small multiple of the grain size. Specifically, it was shown that MEMS devices with dimensions larger than 15x15 grains can be described by using the isotropic properties reported in literature and presented in this report.

The enhanced properties of ta-C presented in this final performance report make it suitable for critical military and civilian applications, such as acoustic emission microsensors for health monitoring of aircraft and nuclear weapon systems, vibration monitoring devices and acoustic signature detectors, micro accelerometers and gyroscopes for inertial guidance, surface acoustic wave devices for gigahertz frequency telecommunications, pressure transducers, and microwave signal generators.

## **ACKNOWLEDGEMENTS**

The PI and his graduate students supported by this program gratefully acknowledge the support provided by the Air Force Office of Scientific Research (AFOSR) through grant F49620-03-1-0080 with Dr. B.L. Lee as the program manager. They also thank their collaborators Drs. T.A. Friedmann, and J.P. Sullivan at the Sandia National Laboratories who provided all ta-C test samples and whose work at Sandia was supported by the U.S. DOE under contract DE-AC04-94AL85000 through the Laboratory Directed Research and Development Program, SNL. The graduate students Ms. Amanda McCarty and Mr. Krishna Jonnalagadda were also supported in part by the National Science Foundation (NSF) under grant CMS-0301584.

## PUBLICATIONS

### Book Chapters:

1. I. Chasiotis, "Experimental Mechanics for MEMS and Thin Films: Direct and Local Sub-Micron Strain Measurements", in *Micromechanics and Nanoscale Effects: MEMS, Multi-Scale Materials and Micro-Flows*, Editor(s): V. M. Harik and L.-S. Luo, Kluwer Academic Press, pp. 3-37, (2004).

### Refereed Publications:

- [1] K. Jonnalagadda, and I. Chasiotis, "Mode I and Mixed Mode Fracture Toughness of Amorphous and Polycrystalline Materials for MEMS", in preparation for *International Journal of Fracture* (2007).
- [2] S.W. Cho and I. Chasiotis, "Elastic Properties and Representative Volume Element of Polycrystalline Silicon for MEMS," to appear in *Experimental Mechanics* **47** (1), (2007).
- [3] S.W. Cho, K. Jonnalagadda, and I. Chasiotis, *Invited Paper*: "Mode I and Mixed Mode Fracture of Polysilicon for MEMS," to appear in *Fatigue and Fracture of Engineering Materials and Structures*, (2007).
- [4] I. Chasiotis, S.W. Cho, and K. Jonnalagadda, "Fracture Toughness and Subcritical Crack Growth in Polycrystalline Silicon", *Journal of Applied Mechanics* **73** (5), pp. 714-722, (2006).
- [5] A. McCarty and I. Chasiotis, "Description of Brittle Failure of Non-uniform MEMS Geometries", to appear in *Thin Solid Films* (2006). (available online)
- [6] S.W. Cho, I. Chasiotis, T.A. Friedman, and J. Sullivan, "Direct Measurements of Young's Modulus, Poisson's Ratio and Failure Properties of ta-C MEMS", *Journal of Micromechanics and Microengineering* **25** (4), pp. 728-735, (2005).
- [7] S. Cho, J.F. Cárdenas-García, and I. Chasiotis, "Measurement of Nano-displacements and Elastic Properties of MEMS via the Microscopic Hole Method", *Sensors and Actuators A Physical* **120**, pp. 163-171, (2005).
- [8] K. Jonnalagadda, S. Cho, I. Chasiotis, T.A. Friedman, and J. Sullivan, "Film Thickness Effect on the Fracture Toughness of Tetrahedral Amorphous Diamond-like Carbon", submitted to *Journal of the Mechanics and Physics of Solids*, (2005).
- [9] I. Chasiotis, *Invited Paper*: "Mechanics of Thin Films and Microdevices", *IEEE Transactions of Devices, Materials, and Reliability* **4** (2), pp. 176-188, (2004).
- [10] I. Chasiotis, S. Cho, and K. Jonnalagadda, "Direct Measurements of Fracture Toughness and Crack Growth in Polysilicon MEMS", *Proceedings of the Materials Research Society* **854E**, pp.U.10.6.1- U.10.6.6, (2005).
- [11] K. Jonnalagadda, S. Cho, I. Chasiotis, T.A. Friedman, and J. Sullivan, "Mode-I Fracture Toughness of Tetrahedral Amorphous Diamond-like Carbon (ta-C) MEMS", *Proceedings of the Materials Research Society* **854E**, pp.U.9.7.1- U.9.7.6, (2005).
- [12] I. Chasiotis, S. Cho, T.A. Friedman, and J. Sullivan, "Young's Modulus, Poisson's Ratio, and Nanoscale Deformation Fields of MEMS Materials", *Proceedings of the Materials Research Society* **795**, Boston, MA, pp. U.10.9.1- U.10.9.6, (2004).

- [13] J.F. Cárdenas-García, S. Cho, and I. Chasiotis, "Thin Film Material Parameters Derived from Full Field Nanometric Displacement Measurements in Non-uniform MEMS Geometries", *Proceedings of the Materials Research Society* **795**, Boston, MA, pp. U.11.28.1- U.11.28.6, (2004).

#### **Ph.D. and Masters Theses supported by this program**

- [1] Sung Woo Cho, *Ph.D. Dissertation*, University of Virginia, defended: August 21, 2006  
[2] Amanda McCarty, *M.S. Dissertation*, University of Virginia, defended: May 5, 2005

#### **Personnel supported**

1. Ioannis Chasiotis, Faculty and PI, University of Illinois at Urbana-Champaign
2. Krishna Jonnalagadda, Ph.D. student, University of Illinois at Urbana-Champaign
3. Sung Woo Cho, Ph.D. student, University of Virginia. Defended: August 21, 2006
4. Amanda McCarty, M.S. student, University of Virginia. Defended: May 5, 2005

#### **Interactions and Transitions to National and Government Laboratories**

- [1] **Data transfer to Sandia National Laboratories:** POC: Dr. T.A. Friedmann, Sandia National Laboratories, Albuquerque, New Mexico 87185, E-MAIL: tafried@sandia.gov
- [2] **Transition of test apparatus to Army Research Laboratory:** Requested on (12/07/2006) by Dr. Tusit Weerasooriya, AMSRD-ARL-WM-TD (B4600), Impact Physics Branch, Army Research Laboratory, Aberdeen Proving Ground, MD 21005, Phone: (410)306-0969, E-MAIL: [tusitw@arl.army.mil](mailto:tusitw@arl.army.mil)
- [3] **Twelve presentations at Conferences, Workshops, and Universities and equivalent number of Conference Publications:** These presentations include 4 invited presentations and one plenary conference presentation.

#### **Honors/awards received during grant lifetime**

- [1] Featured article in April 2005 issue of *Journal of Micromechanics and Microengineering*  
**Honor/Award Recipient:** Chasiotis and S.W. Cho, **Awarding Organization:** *Institute of Physics* ([www.iop.org/EJ/journal/-page=featured/0960-1317/1](http://www.iop.org/EJ/journal/-page=featured/0960-1317/1))
- [2] Best Research Paper Award at the 6<sup>th</sup> International Symposium on MEMS and Nanotechnology, Annual Meeting of the Society for Experimental Mechanics, Portland, OR (6/2005), **Honor/Award Recipient:** I. Chasiotis, S.W. Cho, and J. Cardenas. **Awarding Organization:** *Society for Experimental Mechanics*.

## DETAILED TECHNICAL DESCRIPTION OF RESEARCH

### **I. Young's modulus, Poisson's ratio, and tensile strength of MEMS materials (YEARS 1-2)**

In the first two years of this project a novel method to measure full-field in-plane strain in thin films with true nanometer resolution was developed. The method employed Atomic Force Microscopy (AFM) images of the surface of thin films and combined those with Digital Image Correlation (DIC) to extract strains. Figure 1 shows a flow chart of the measurement method [1].

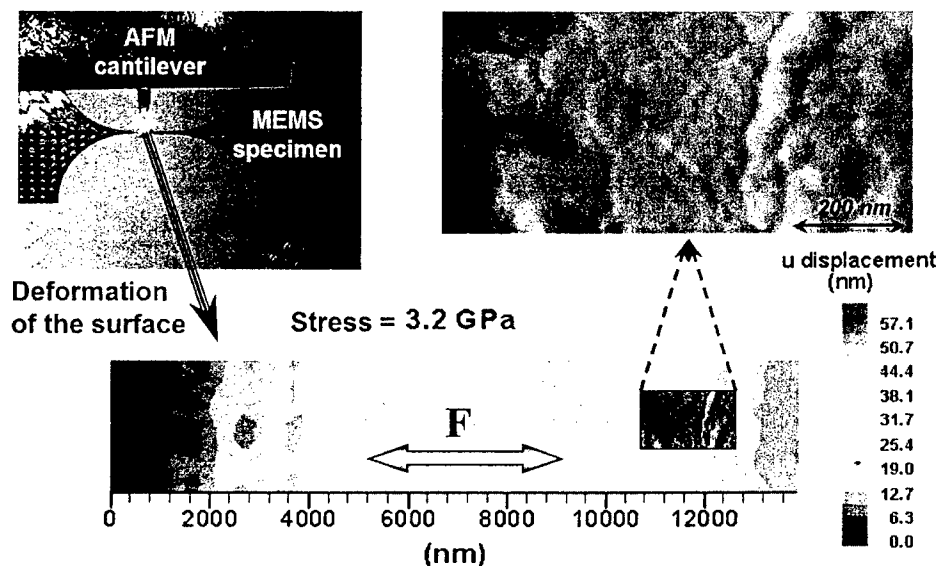


**Figure 1.** Displacement field measured directly at the specimen gage section and detail of local deformation in  $0.5 \times 1 \mu\text{m}^2$  material domain that shows strain localization in individual grains. In the top right image the displacement contour is superposed on the topographic image of the specimen [1,2,3]. Contour images are best viewed in color.

### **MEMS Materials investigated under this AFOSR program**

The materials used in this AFOSR sponsored program were polycrystalline silicon (polysilicon) and tetrahedral amorphous diamond-like carbon (ta-C). Polysilicon samples were manufactured at two established MEMS fabrication facilities using the Multi-user MEMS Processes (MUMPs) [4] and the Sandia Ultra planar four layer Multilevel MEMS Technology (SUMMiT IV) process [5] to ensure good film quality, small defect density, and dimensional accuracy. Before this research program very limited information was available about the elastic modulus and none about Poisson's ratio for SUMMiT polysilicon or ta-C. Furthermore, there was no comparative study of the mechanical properties of polysilicon from the two processes using the same experimental method, while the applicability of these effective properties to components whose size is only a few microns was unknown.

The second material for MEMS that was investigated during this research program was ta-C. The latter were deposited at room temperature using pulsed-laser deposition (PLD) with a KrF excimer laser source (248 nm) and a rotating solid pyrolytic graphite target at  $10^{-7}$  Torr



vacuum. The growth conditions were set to those that typically produce high 4-fold content (~80%) ta-C thin films. The high compressive residual stresses developed during deposition were completely relieved by subsequent thermal annealing for several minutes in a rapid thermal annealing oven purged by an inert gas (Ar) at 600-650 °C [6]. The final ta-C MEMS structures were fabricated via conventional semiconductor processing techniques [7]. Briefly, the surface of the ta-C films was patterned with an aluminum hard mask using lift-off. The resulting patterned structures were dry etched in a commercial etch tool by an oxygen plasma and undercut using a timed HF acid etch of the underlying sacrificial SiO<sub>2</sub> layer.

### **Experimental Details**

The test apparatus employed in this program was designed and implemented based on prior work by the PI that was also supported by AFOSR and reported in [1]. The specimens were gripped using a UV-curable adhesive applied on a flat glass grip to load MEMS specimens. The thin glass grip was attached to piezoelectric actuator with 1 nm precision in motion while the other end of the specimen was attached to a commercial load cell with 0.5 N capacity and better than 0.5 mN resolution. The test apparatus was integrated with a commercial AFM that was outfitted with a hardware correction system for linearization of the piezoelectric actuator motion. The entire test system was installed in a thermally and acoustically isolated chamber. To avoid potential vibrations induced by the AFM cantilever probe to the freestanding specimens, intermittent soft (low force) tapping mode was employed to minimize the force exerted on the specimen during scanning.

Using the AFM/DIC method outlined in Figure 1, full-field displacements were acquired in 5×15 μm<sup>2</sup>, or smaller, regions in microtension specimens and were used to compute the material strain [2,8,9,10]. The application of DIC was conducted using the material surface roughness as distributed markers. The DIC correlation square used to calculate the effective properties in the 5×15-μm<sup>2</sup> AFM images was 20×20 pixels (300×300 nm). The optimum size of the correlation square was determined iteratively. Small sizes that did not contain sufficient surface details resulted in erroneous local displacements while very large correlation squares resulted in smooth displacement contours eliminating local information.

### **Procedures for the calculation of the isotropic elastic constants $E$ and $\nu$**

A set of five AFM images was obtained at each of five or more load levels applied to every specimen and were processed using DIC. Figure 2 shows a sequence of axial and transverse displacement contours and the applied stresses. The contour legends were adjusted to the displacement range in the highest load. The  $u$  and  $v$  displacements were obtained from AFM images with fast scanning directions along the  $x$ - and the  $y$ -axis, respectively. The axial and transverse displacements were quite uniform in 5×15-μm<sup>2</sup> fields sampled at different locations on the specimen, which is expected in a uniaxial tension test. Thus, polysilicon-specimens of this size behaved homogeneously and in a linearly elastic manner. As will be explained later, a 15×15-μm<sup>2</sup> specimen area is a Representative Volume Element (RVE) for polysilicon.

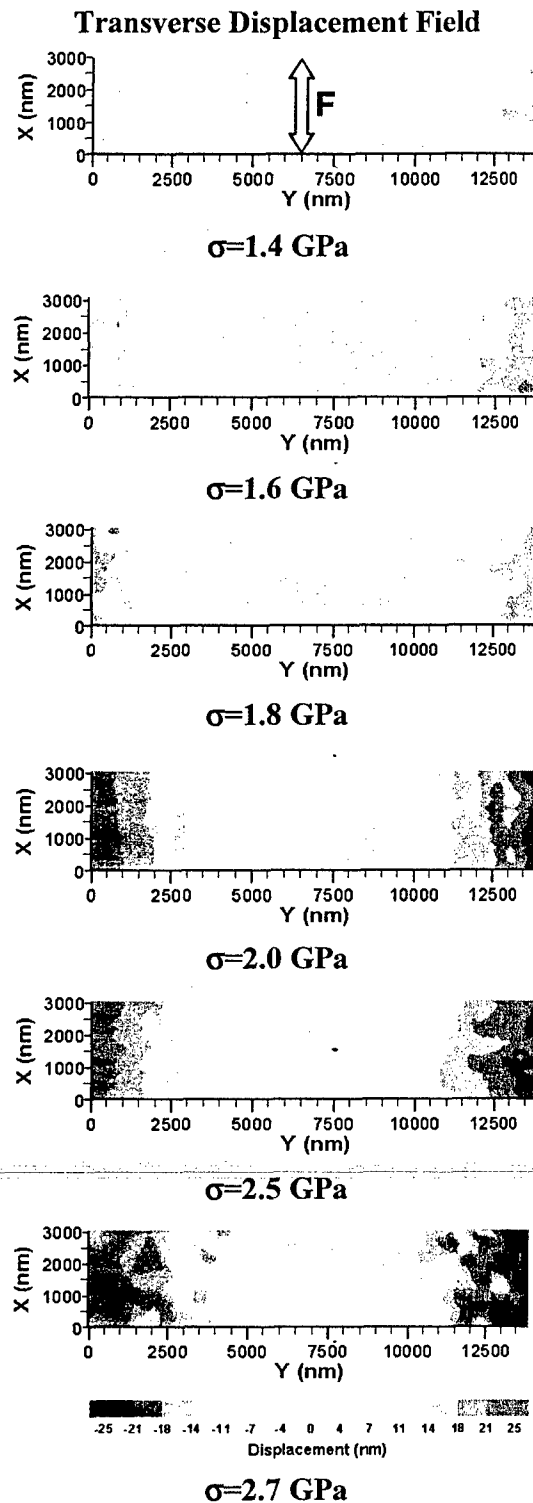
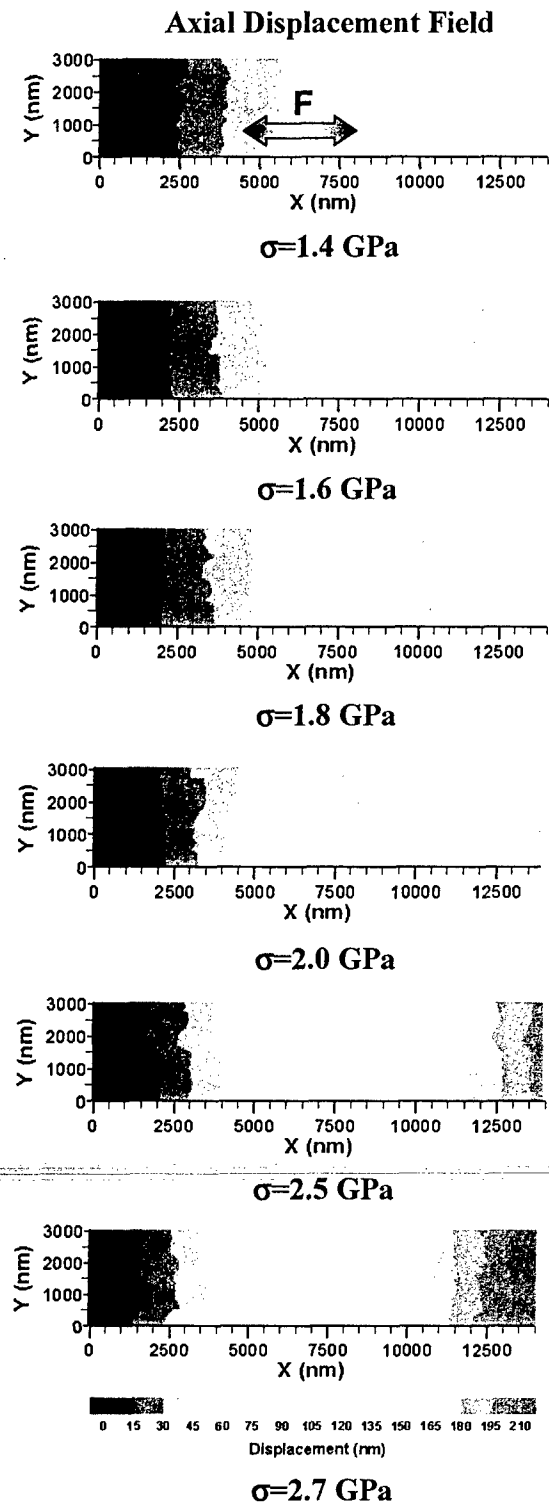


**Figure 2.** Axial and transverse displacement fields in a  $5 \times 15\text{-}\mu\text{m}^2$  area of a polysilicon specimen from SUMMIT. These sets of images were used to measure the Young's modulus and Poisson's ratio of polysilicon. Contour images are best viewed in color.

The average axial and transverse strains at each applied stress were obtained as the average slope of all horizontal  $u$ -contour lines in Figure 2. The average axial strain in each contour was obtained from the line fits. Subsequently, the strains from 25 contour images per load level were averaged<sup>1</sup>. Two line fits from the axial and transverse displacement contours at 2.5 GPa applied stress are shown in Figures 3(a,b). In a linearly elastic material the local displacement as a function of position yields a straight line whose slope  $du/dx$  is the line strain. The calculation of the average strain by this approach was more consistent compared to the local  $du/dx$  computed by DIC, or by point-by-point differentiation of the displacement field. Averaging of the latter full-field strains could remove random noise and provide uniform strains but the displacement data required smoothing that would make this analysis subjective. The average strain at each load was used to construct the stress-strain curves as shown in Figure 4. The nominal stress was calculated from the readings of the load cell. Although the number of points was small due to the time required for AFM imaging, all points fit a straight line very well whose slope is the Young's modulus.

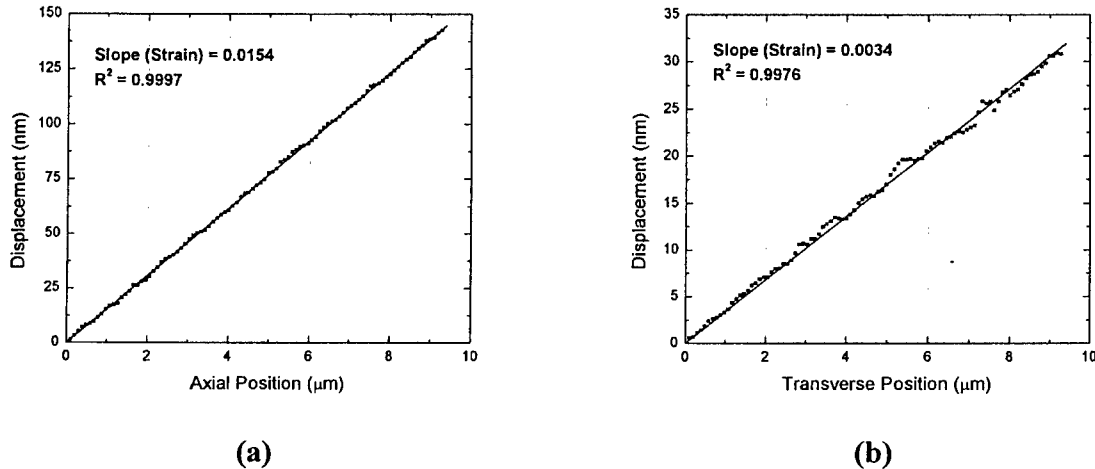


**Figure 3.** Local displacement as a function of position in the (a) axial and (b) transverse direction. The data lines were derived from the contours in Figure 2 at 2.5 GPa applied stress. The zero displacement was arbitrarily set at the origin of the coordinate system.

The average elastic modulus for MUMPs 41 run was  $164 \pm 7$  GPa which agreed well with the value of 165.7 GPa reported before [1] using cross-head measurements that accounted for the apparatus compliance. The elastic modulus for the SUMMiT polysilicon was  $155 \pm 6$  GPa, which was in good agreement with the effective modulus of  $164 \pm 3$  GPa reported in [11]. On the other hand, the Poisson's ratio was not been reported before for either process or obtained at this scale. Using the full-field axial and transverse deformation data, the Poisson's ratio was found to be virtually the same for both processes averaging  $0.219 \pm 0.018$  and  $0.224 \pm 0.017$  for MUMPs and SUMMiT-IV, respectively. These values agreed with measurements conducted on MUMPs

<sup>1</sup> When optical microscopy is used it is customary to average images before conducting DIC so that fluctuations in the pixel gray level intensity are minimized. This is not possible with AFM images because of the small rigid body displacements that occur between consecutive images.

polysilicon at the same scale using inverse solutions to deduce the elastic properties as described in the next section [12,13]. This calculation of Poisson's ratio was independent of the measurement of the applied load. Moreover, these strain measurements were insensitive to the calibration of the AFM. Raw AFM data given in pixels were used and the entire calculation was conducted in terms of pixels. For convenience, all data in this final progress report are presented in physical dimensions, i.e. nanometers or microns.

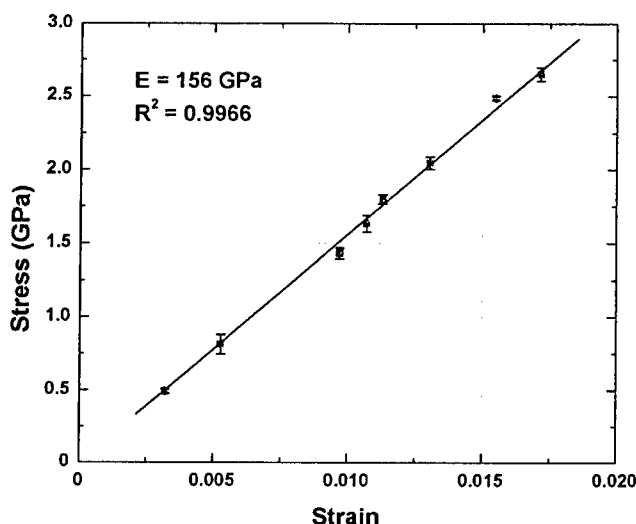


**Figure 4.** Stress-strain curve calculated from the displacement contours in Figure 2. Each point is the average of the strain measured from 25 contour plots. The error bars for strain were too small to be shown.

be discussed in a later section of this report, the material strength did differ significantly between the two processes and ta-C because of the existence of very different types of flaw populations that were the result of the various fabrication processes. The procedures for the measurement on the elastic and failure properties of ta-C were the same as those for polysilicon and were summarized by the PI and his group in reference [10].

Table I summarizes the experimental results. The difference in the elastic properties between the two processes was ~5% or less, while the mechanical strength differed by as much as 60% with the SUMMIT-IV results taken as the reference. The large deviation in strength was attributed to the high surface roughness of MUMPs polysilicon that generated distributed surface notches. The results, presented in Table I, are very consistent i.e. there is very small standard deviation. Measurements of the elastic material properties for polycrystalline silicon originating from different sources (Sandia and MCNC-Cronos) have shown that the elastic properties of polysilicon MEMS with similar microstructure differ very little. As will

**Table I.** Elastic and failure properties of polysilicon and ta-C MEMS [2,8,9,10].

	Young's Modulus (GPa)	Poisson's Ratio	Tensile Strength (GPa)	Weibull Parameters m=Weibull modulus $\sigma_0$ = stress parameter
Polycrystalline Silicon (SNL)	156±6	0.225±0.01	3.15±0.45	m = 6-18, $\sigma_0$ = 3.0-3.5 GPa
Polycrystalline Silicon (MUMPs)	165±6	0.22±0.01	1.75±0.2	N/A
ta-C	756±22	0.16±0.03	7.1±0.5, (11.4±0.8)	m = 6, $\sigma_0$ = 7.6 GPa

### Application of AFM/DIC method in inverse problems

The AFM/DIC method was employed to record deformation fields in very small material domains that were subject to non-uniform stress fields. As seen in Figure 5, displacement fields were obtained in the vicinity of 6  $\mu\text{m}$  circular perforations located at the gage section of a polycrystalline silicon tension specimen [12,13]. The maximum line displacement in Figure 5 is only 2.4 data pixels (36 nm) at the lower end of the contour and 1.6 data pixels (24 nm) at the upper end of the image. This displacement field was used to calculate the elastic properties of polysilicon by solving the inverse problem of a hole in a plate and fitting the AFM/DIC data to an analytical model using a least square minimization scheme of  $f_k$  such that

$$f_k(E, \nu) = \left[ (u_r)_k \cos \theta_k - (u_\theta)_k \sin \theta_k \right]_{\text{theoretical}} - \left[ (u_x)_k \right]_{\text{measured}} = 0 \quad (1)$$

in which,

$$(u_r)_k = \frac{S(1+\nu)}{2Er_k} \left[ \left( \frac{1-\nu}{1+\nu} \right) r_k^2 + a^2 + \left( \frac{4a^2}{1+\nu} + r_k^2 - \frac{a^4}{r_k^2} \right) \cos 2\theta_k \right] \quad (2)$$

and,

$$(u_\theta)_k = -\frac{S(1+\nu)}{2Er_k} \left[ \left( \frac{1-\nu}{1+\nu} \right) 2a^2 + r_k^2 + \frac{a^4}{r_k^2} \right] \sin 2\theta_k \quad (3)$$

Using equations (1-3) and the data in Figure 5 the elastic modulus of polysilicon was calculated as 160 GPa, which was in excellent agreement with the value listed in Table I measured from uniform tension samples [13]. This presents an alternative approach to calculate the elastic constants of linearly elastic MEMS materials by using a single displacement field. Since the elastic properties were accurately recovered from the recorded deformation field, the associated notch sensitivity factor is equal to one.

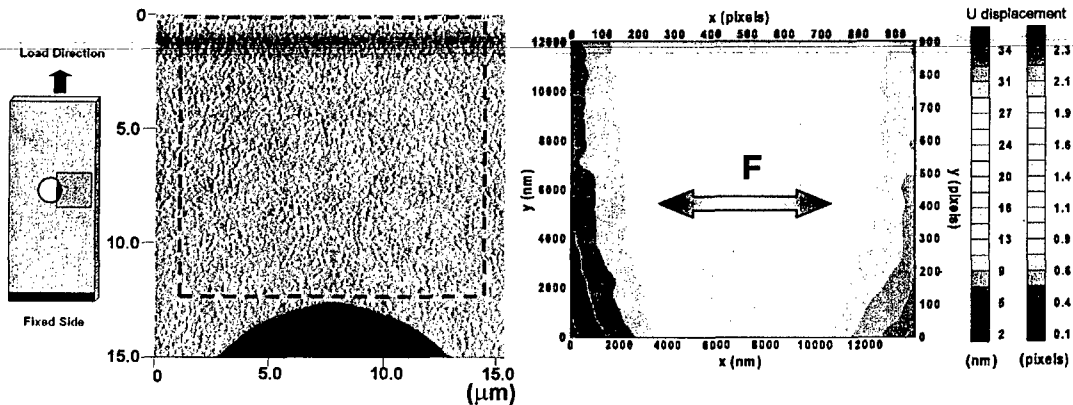


**Figure 5.** Displacement field in the vicinity of a circular notch and in the direction of the applied load. The notch is located at position (7000, -500) nm with respect to the coordinate system of the contour plot. The maximum line displacement near the notch is only 2.4 data pixels (36 nm) [12,13]. Contour images are best viewed in color.

## II. Limitations imposed by device size in the use of effective elastic properties (YEARS 2-3)

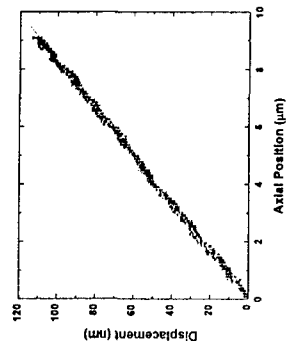
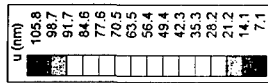
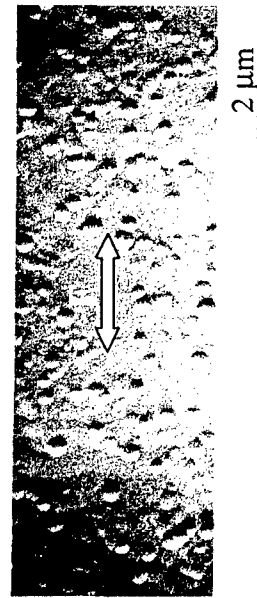
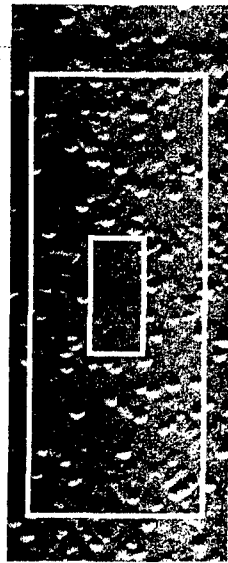
Due to *grain anisotropy and polycrystalline inhomogeneity*, the properties in Table I, although valid for specimen sizes  $5 \times 15 \mu\text{m}^2$  or larger, may not describe appropriately the effective mechanical behavior of smaller size specimens. Polysilicon is modestly anisotropic,  $130.2 < E < 187.9$  GPa in [100] and [111] directions, respectively [14], while according to [15] when the specimen contains less than 200 grains crystalline anisotropy becomes important resulting in statistical variation of the measured properties.

The AFM/DIC method was applied to determine the smallest specimen size (RVE) whose effective mechanical behavior could be described by the isotropic properties of SUMMIT-IV polysilicon in Table I. Because it was shown that a  $15 \times 15 \mu\text{m}^2$  specimen is described well by these properties, smaller domain sizes were employed. Furthermore, the deviation from homogeneity<sup>2</sup> is of stochastic nature and it depends on the location on the sample. In this section of the report one typical specimen area and one area that resulted in the large deviation from the homogeneous case are presented. The material structure is assumed to be columnar which in general is a fair assumption. The first example (Figures 6 and 7) involved six mutually inclusive domains with dimensions of  $1 \times 2 \mu\text{m}^2$ ,  $1.5 \times 3 \mu\text{m}^2$ ,  $2 \times 4 \mu\text{m}^2$ ,  $3 \times 6 \mu\text{m}^2$ ,  $4 \times 8 \mu\text{m}^2$ , and  $5 \times 10 \mu\text{m}^2$ . In the second example (Figure 8) three mutually inclusive domains with dimensions of  $1 \times 2 \mu\text{m}^2$ ,  $2 \times 4 \mu\text{m}^2$ , and  $5 \times 10 \mu\text{m}^2$  were imaged by an AFM. Further details are provided in reference [3].

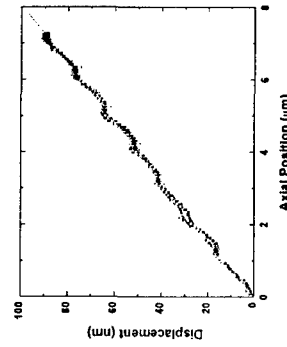
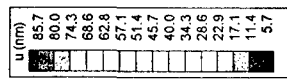
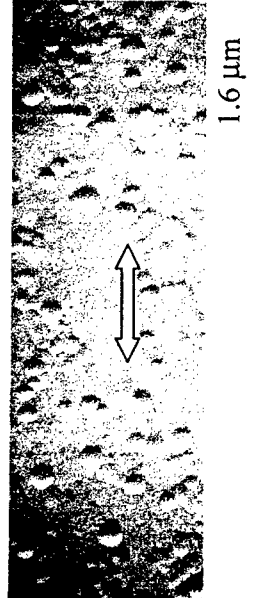
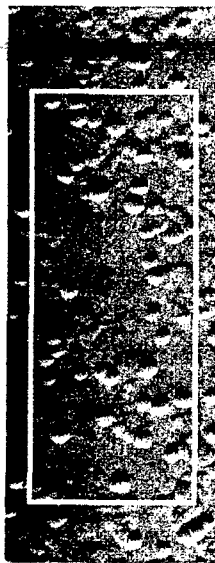
Figure 6 (left) shows the reference AFM images with 1024 pixel line resolution. The superimposed  $u$ -displacement contours on the AFM images are also shown to identify correlations between local deformation and grain structure. On the right, the local  $u$ -displacement as a function of axial specimen location is plotted for 16-20 lines of the displacement contours. The straight line in each plot is the average of the best-fit lines to all experimental displacements and its slope is used as a measure of the average strain in the specimen. The combined displacement contour/AFM topographic image of the largest area shows linearly varying axial displacements according to linear elasticity. The smaller fields of view are associated with increasing non-uniformity in displacement distribution compared to the  $5 \times 10 \mu\text{m}^2$  AFM image. The smaller specimen domains,  $1.5 \times 3 \mu\text{m}^2$  and  $1 \times 2 \mu\text{m}^2$ , demonstrated the highest scatter in the axial displacement distribution. In images 6(e,f) the local deformations follow the material microstructure. A more accurate picture is provided by the line displacement plots that are very linear in large specimen areas. The deviation from linearity was pronounced in the smaller images being maximum in the  $1 \times 2 \mu\text{m}^2$  domain. The correlation coefficient,  $R^2$ , for the line plots in Figure 6(c) varied from 0.96-0.993 for the smallest and the largest image size, respectively. These values and the average slope of all lines provided a measure for the deviation of the effective deformation of these specimen areas from the RVE. In this analysis the average slope of all displacement lines in each contour was used as a measure of the average strain in the sample as well as the local deformation inhomogeneity. Given this average strain value and the applied far-field stress, the effective elastic modulus for each field of view was computed. This quantity was finally used to determine the deviation of each specimen domain from the RVE whose effective mechanical behavior is characterized by the effective material modulus.

---

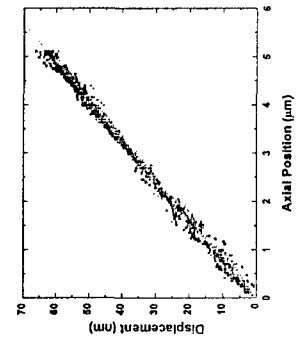
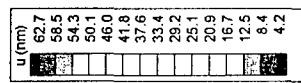
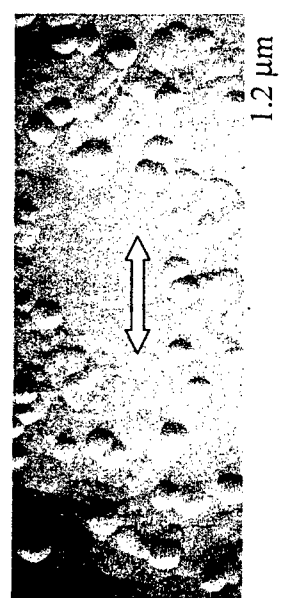
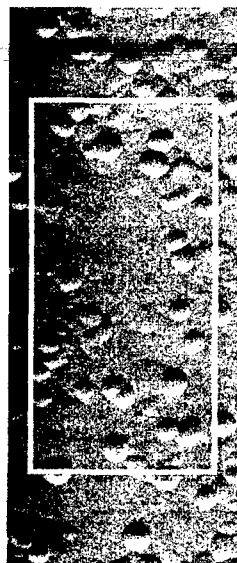
<sup>2</sup> The grain structure of polysilicon is the source of inhomogeneity and as a consequence the reason for deviation from isotropy.



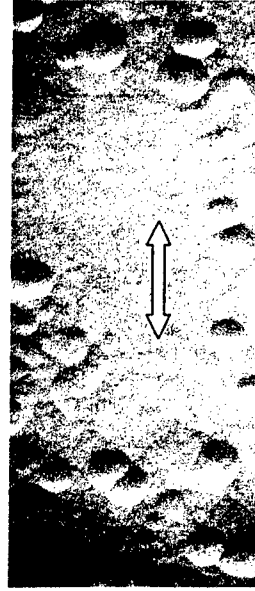
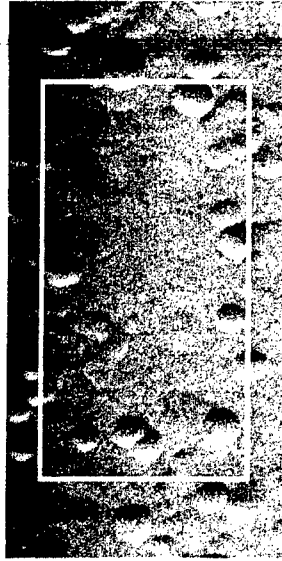
(a)  $5 \times 10 \mu\text{m}^2$



(b)  $4 \times 8 \mu\text{m}^2$

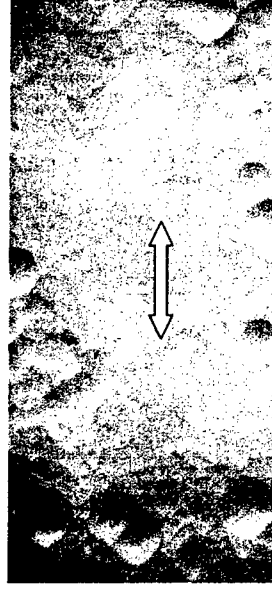
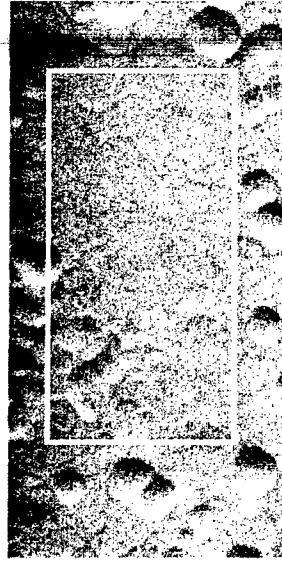
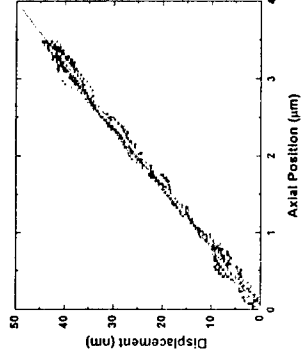
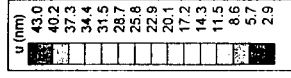


(c)  $3 \times 6 \mu\text{m}^2$



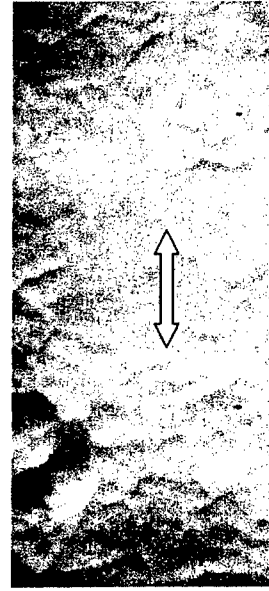
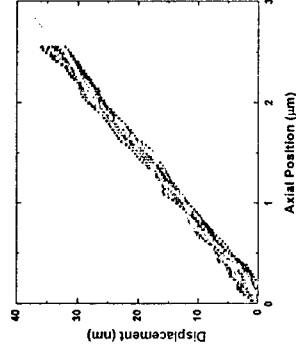
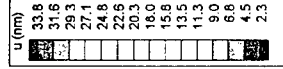
800 nm

(d)  $2 \times 4 \mu\text{m}^2$



600 nm

(e)  $1.5 \times 3 \mu\text{m}^2$



400 nm

(f)  $1 \times 2 \mu\text{m}^2$

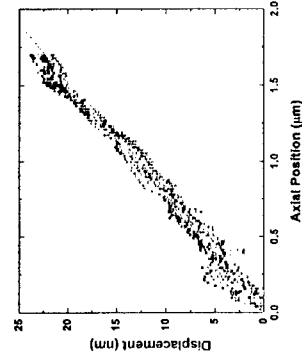
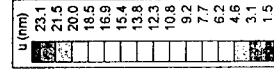




**Figure 6. (Left)** AFM images of (a)  $5 \times 10 \mu\text{m}^2$ , (b)  $4 \times 8 \mu\text{m}^2$ , (c)  $3 \times 6 \mu\text{m}^2$ , (d)  $2 \times 4 \mu\text{m}^2$ , (e)  $1.5 \times 3 \mu\text{m}^2$ , and (f)  $1 \times 2 \mu\text{m}^2$  areas in a  $2.5 \mu\text{m}$  thick polycrystalline silicon specimen subject to uniaxial tension. The areas marked by rectangles in (a-e) are images (b-f) respectively. The small rectangle in image (a) is image (f). All AFM images have the same pixel resolution. **(Center)**  $u$  displacements superposed on the grain structure. **(Right)** Plots of the local  $u$ -displacement as a function of axial position. There is a direct correlation between local displacements and grain inhomogeneity for (e)  $1.5 \times 3 \mu\text{m}^2$ , and (f)  $1 \times 2 \mu\text{m}^2$  areas. The periodic steps in the line plots in Figure 6(b) are experimental artifacts that were not filtered out to preserve the data scatter. Contour images are best viewed in color [3].

The moduli computed from Figures 6(a-f) and the associated standard deviations are plotted in Figure 7. The shaded area designates the isotropic modulus and its standard deviation in Table I. The calculated effective modulus varied with the domain size demonstrating a systematic trend to the isotropic behavior for larger specimens areas. The maximum standard deviation was computed for the smallest domain size while it became minimum for the largest domain size. The modulus trend towards the isotropic behavior was not monotonic. There were small domains ( $1.5 \times 3 \mu\text{m}^2$ ) whose effective mechanical response was closer to that of an RVE and relatively larger domains ( $2 \times 4 \mu\text{m}^2$ ) with larger deviation from the effective behavior. The minimum specimen area that provided an effective elastic modulus within the bounds of the measurements from the  $5 \times 15 \mu\text{m}^2$  material domains was equal to  $5 \times 10 \mu\text{m}^2$ . The effective elastic modulus measured from contour 6(a) was  $160 \pm 2$  GPa, it agreed with the average in Table I ( $155 \pm 6$  GPa). Thus, a  $5 \times 10 \mu\text{m}^2$  specimen area is an RVE for polysilicon. This RVE size was confirmed by additional measurements on SUMMIT-IV polysilicon.

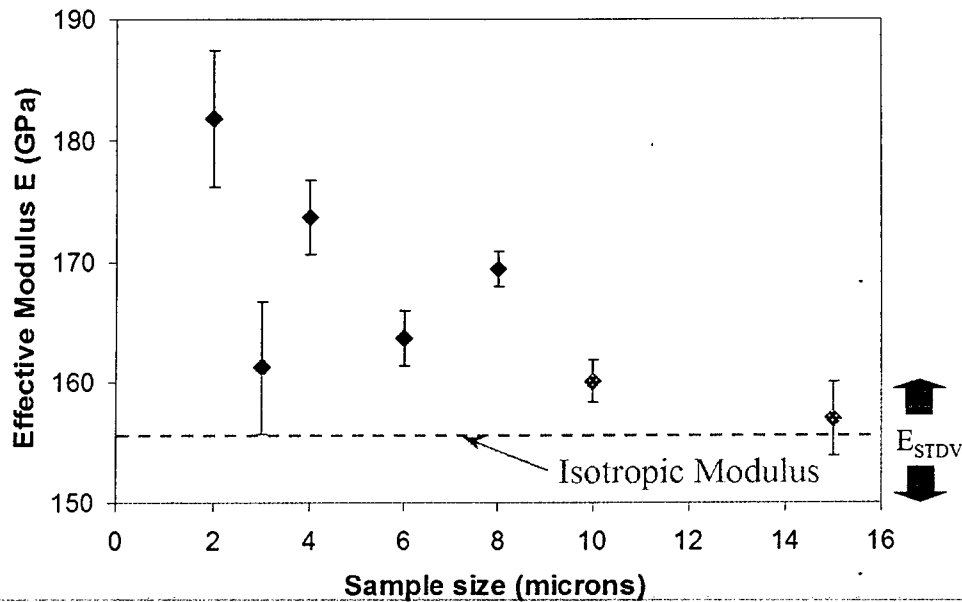


**Figure 7.** Effective modulus as a function of domain size. The error bars are the standard deviation from the line plots in Figure 6. The shaded area corresponds to the isotropic modulus with one standard deviation.

The plots in Figure 6 provided a rather conservative picture of the effect of material inhomogeneity. An example of local displacements that deviate significantly from a uniform distribution is provided in Figure 8. Three images sizes with dimensions  $1 \times 2 \mu\text{m}^2$ ,  $2 \times 4 \mu\text{m}^2$ , and  $5 \times 10 \mu\text{m}^2$  were obtained. Contrary to Figures 6(d,f), the displacement non-uniformity in  $2 \times 4 \mu\text{m}^2$  and  $1 \times 2 \mu\text{m}^2$  domains was pronounced as local grain inhomogeneity considerably affected the displacement distribution. A quantitative description of the variation of local displacements in the three AFM image sizes is given in the line plots 8(a-c) that show 24, 18, and 17 displacement lines from each contour in Figures 8(a-c) respectively.

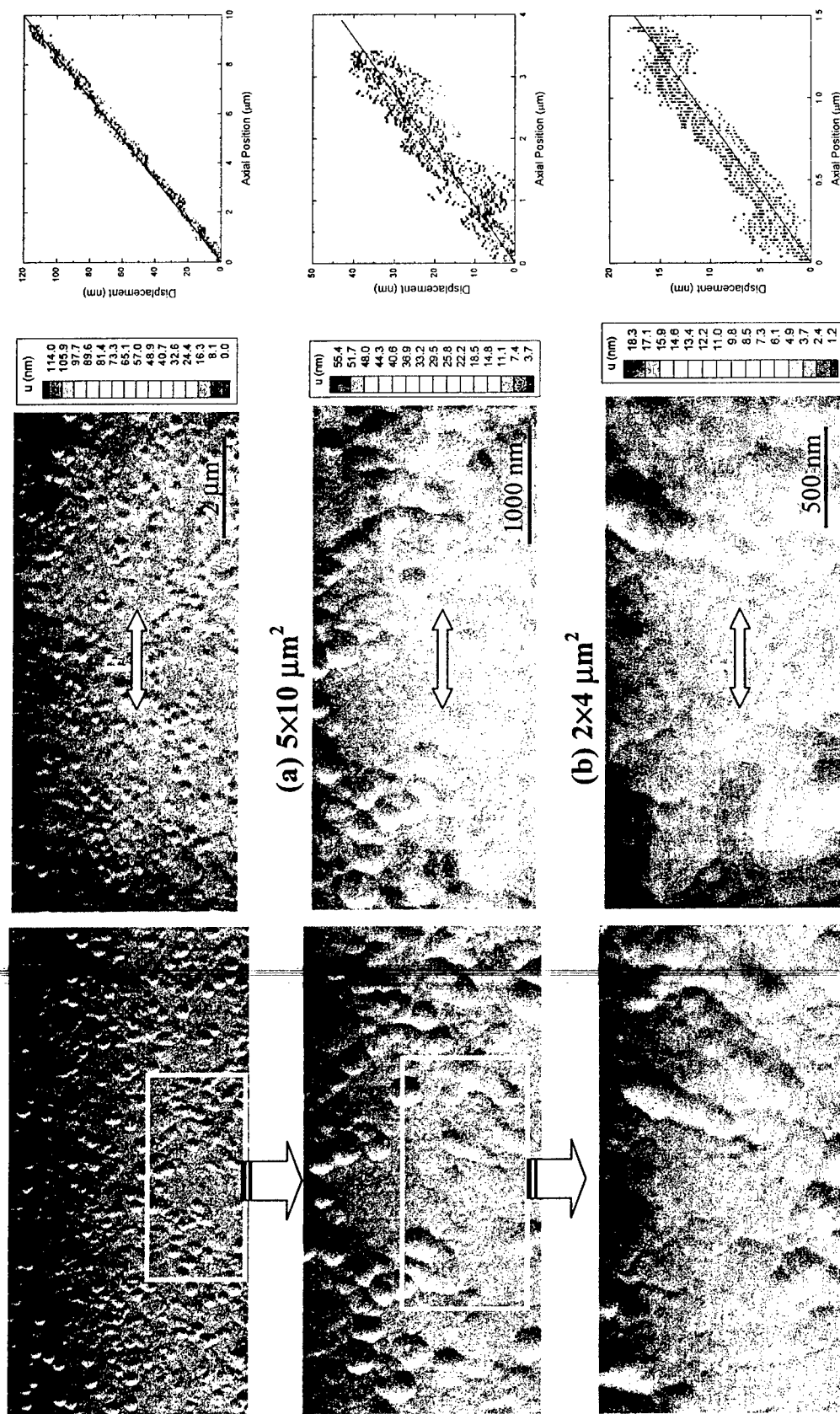


**Figure 8.** (Left) AFM images of (a)  $5 \times 10 \mu\text{m}^2$ , (b)  $2 \times 4 \mu\text{m}^2$ , and (c)  $1 \times 2 \mu\text{m}^2$  areas in a  $2.5 \mu\text{m}$  thick polycrystalline silicon specimen under uniaxial tension. (Center)  $u$  displacement contours superposed on the grain structure. The areas marked by rectangles in (a) and (b) are images (b) and (c) respectively. All AFM images have the same pixel resolution. There is a direct correlation between local displacements and grain inhomogeneity for (b)  $2 \times 4 \mu\text{m}^2$ , and (c)  $1 \times 2 \mu\text{m}^2$  areas. (Right) Plots of the local displacement as a function of position for each material domain extracted from the contour plots. The straight lines show the isotropic behavior and are not data fit lines.

Based on this analysis it is concluded that the effective mechanical behavior of polysilicon samples equal or larger than  $10 \times 10 \mu\text{m}^2$  is described by the effective properties. Given the 650 nm average grain size of SUMMiT polysilicon, a material domain that includes  $15 \times 15 = 225$ , or more, columnar grains behaves isotropically with a statistical scatter of less than 5%. This experimental assessment of the RVE is in agreement with computational results in [15] for  $\langle 100 \rangle$  textured polysilicon. It also provides a measure of the number of grains in the RVE rather than an absolute length scale which could be used to obtain estimates for the physical size of an RVE of polysilicon with different grain size but the same grain structure and orientation distributions as the samples used here. Along the same lines are the results of the analysis in [16] which concluded that for many cubic materials the RVE is at most 20 times the grain size. It is characteristic that analogous results were obtained before for macroscopic polycrystals, such as columnar ice, with grain structure similar to polysilicon. Specifically, [17] showed that 300 grains are sufficient to bring the elastic modulus of S2 ice within the Voigt-Reuss bounds that are meaningful for a statistically homogeneous solid and thus 300 grains would constitute an RVE.

The description of material deformations under non-uniform stresses using isotropic properties deserves special attention, as larger domain sizes may be required to capture the smooth strain gradients in MEMS designs with acute notches or sharp corners. As was shown in a previous section, the displacement field in a  $15 \times 15 \mu\text{m}^2$  area next to a circular hole with a modest stress concentration factor of  $K=3$  and a diameter of  $6 \mu\text{m}$  follows that described by the isotropic elastic constants [13]. The specimens were fabricated by the MUMPs 41 process and the grain size was half of that for SUMMiT polysilicon. Using the displacement field and the solution to the inverse hole problem the Young's modulus and the Poisson's ratio of MUMPs polysilicon were determined to be in very good agreement with those from uniform tension tests that are reported in Table I. Furthermore, a study of the fracture of MUMPs polysilicon involving mode I loading of mathematically sharp cracks [18] showed that  $15 \times 15 \mu\text{m}^2$  experimental crack tip displacement fields compared well with the analytical solution (see later Figure 13) assuming isotropy and the elastic properties in Table I. Thus, even in the presence of high strain gradients, the linear elastic constants can describe  $15 \times 15 \mu\text{m}^2$ , or larger, specimens sufficiently well. These results should be compared with the RVE for MUMPs polysilicon that could be inferred from the measurements presented here. Using the estimated RVE size for SUMMiT polysilicon, the RVE for MUMPs polysilicon containing  $15 \times 15 = 225$  grains is approximately  $5 \times 5 \mu\text{m}^2$ . Thus, the  $15 \times 15 \mu\text{m}^2$  domains of MUMPs polysilicon used in the fracture and stress concentration measurements were larger than the RVE.

The columnar grain structure is not perfectly regular because of grains that are oriented at non-zero angles with respect to the film normal. Thus, the actual material deformation is rather three-dimensional and the RVE may be larger than estimated here. In any event, polysilicon domains that contain less than  $15 \times 15$  grains should rather be described in terms of property bounds, or by employing a thorough description of the local anisotropic elastic behavior and not the isotropic elastic properties.

### III. Mechanical failure of polysilicon MEMS devices (YEAR 2)

The mechanical failure of polysilicon MEMS was further analyzed using experimental results acquired in a prior work supported by AFOSR [19]. The objective of this part of the research program that resulted in an M.S. thesis [20] was to identify a single pair of Weibull parameters that could describe the failure of a wide number of polysilicon specimen geometries. The study was conducted with the aid of the NASA's code CARES Life (Ceramics Analysis and Reliability Evaluation of Structures Life) and finite element models of perforated MEMS specimens. Using these tools and experimental data from previous studies and newly tested specimens the Weibull stress parameter, a quantity that is independent of specimen geometry, was calculated [21]. Figure 9(a) shows that both the stress concentration factor and the radius of curvature influence the failure strength of a MEMS component. While smaller radii of curvature support higher local stresses, the higher the stress concentration factor the higher the probability of failure for the same local stress and local radius of curvature (i.e. local geometry). These data can be used in device design in place of the most conservative (still size dependent) strength derived from uniaxial tension tests.

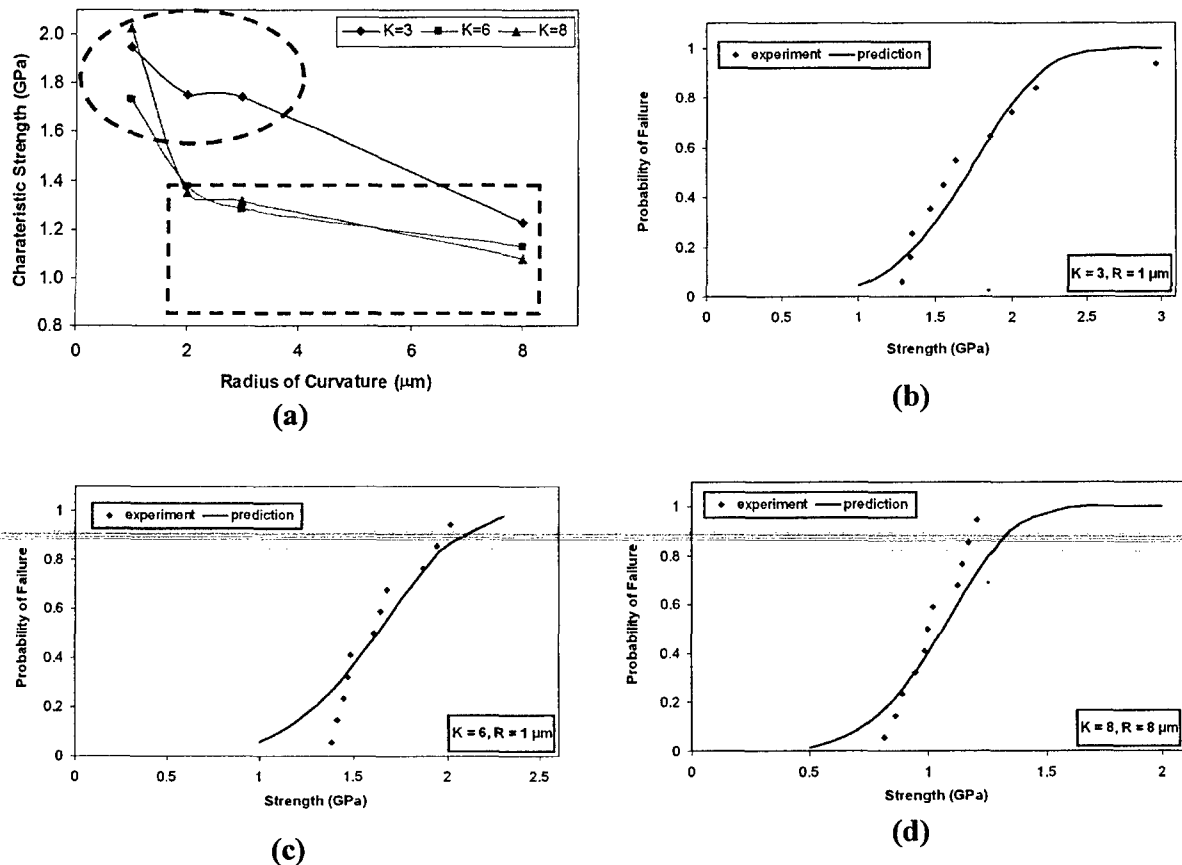


**Figure 9.** (a) Characteristic strength depends on the flaw population. Different geometries activate different flaw populations. Small radii of curvature or small perforations promote failure due to side-wall roughness while large radii of curvature or large holes promote failure that scales with the specimen top surface. (b-d) Calculated probabilities of failure based on the optimum value  $m=5$  of the parametric study for the interior hole surface analysis [21] for (b)  $K=3, R=1 \mu\text{m}$ , (c)  $K=6, R=1 \mu\text{m}$ , and (d)  $K=8, R=8 \mu\text{m}$ .

Then, the accuracy in using a unique set of Weibull parameters in the integral form of the Weibull cumulative distribution function to describe a broad class of specimen geometries was investigated in order to isolate the geometric factor of strength (non-material parameter) from the material factor (material stress parameter) thus eliminating the restriction that Weibull parameters derived with a specific specimen geometry can only be used for similar geometries.

The aforementioned approach was tested using twelve non-uniform MEMS-scale specimens containing a central perforation. The twelve specimen geometries were created using combinations of stress concentration factors and radii of curvature [19]. The integral form of the Weibull cumulative distribution function in conjunction with a finite element model in ANSYS accounted for the non-uniform stress distribution in each specimen. The material scale parameter and the Weibull modulus were determined for flaw populations scaling with (i) the top specimen surface area and (ii) the sidewall surface area. It was found that for 1-3  $\mu\text{m}$  radius circular perforations ( $K=3$ ) the active flaw population scaled with the size of the specimen top surface and failure was attributed to the surface roughness, as was the case for uniform tension specimens. For higher stress concentration factors ( $K=6$  and 8), the local material strength scaled with the interior sidewall surface of the perforation. *Our analysis resulted in twice the accuracy of predicted strength distributions compared to prior works [21].*

Predictions and experiments of three different geometries are presented in Figures 9(b-d). A single set of Weibull parameters provided accurate descriptions only in the case of consistent flaw population [21]. In reference to Figure 9(a) the analysis conducted in this project points to the realization that the characteristic strengths with high values were those measured from failures originating in the specimen sidewall surfaces compared to the smaller characteristic strength values that originated in failures due to the top surface roughness induced flaws. *As a result, extrapolations using Weibull parameters computed using arbitrarily small or large specimens must be done with caution to ensure consistent active flaw population for all specimens even when self-similar specimens are used.*

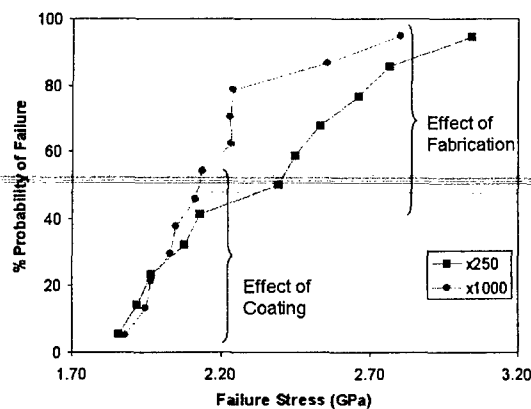


**Figure 10.** Bimodal strength distribution of W-coated polysilicon MEMS. In the upper part of the curve failure was initiated because of microfabrication-induced flaws while for the lower part of the curve the W-coating was responsible for failure [22].

Finally, the failure of Tungsten (W) coated polysilicon MEMS was investigated. W-coatings are used as solid lubricants to reduce wear in polysilicon MEMS by a factor of 10,000. For these samples it was found that a bimodal strength distribution describes the strength data shown in Figure 10 [22]. The 20 nm thick W-coatings decreased the material strength by almost a factor of two. This adverse effect was attributed to W precipitates in Si grains that generate an additional flaw population that is in competition with the existing sidewall flaws that are responsible for failure in Sandia MEMS, hence the bimodal failure distribution in Figure 10, while for part of the data failure scaled with the specimen length as reported before [19] for probabilities of failure <40% the specimens broke due to W-precipitates.

#### IV. Fracture Toughness of Brittle MEMS Materials (YEARS 2 & 3)

The strength data in Table I as explained in the previous section provided a probabilistic view of MEMS failure. A comprehensive investigation of device failure was conducted via experiments with samples containing single large flaws (cracks) that were solely responsible for fracture. Fracture toughness tests with MEMS-scale specimens containing mathematically sharp cracks (Figures 11(a,b)) were conducted to measure the critical stress intensity factors of ta-C and polysilicon [18,23,24,25]. Atomically sharp cracks were introduced with the aid of a micro-hardness tester according to [26] as seen in Figures 11(a-d). Indentations were created with a Vickers indenter at a distance of 20-30  $\mu\text{m}$  from specimens deposited and patterned on a 2  $\mu\text{m}$   $\text{SiO}_2$  blanket layer on a silicon chip. The cracks emanating from the corners of the indenter propagated in the substrate and into the tensile specimen, Figure 11(b), providing a sharp crack that was used to measure the material fracture toughness. After the crack propagated into the gage section (Figure 11(b)) the polysilicon specimen was removed from its substrate, Figure 11(c), and a fracture test was conducted. AFM topographic records, taken before the specimen was released from its substrate, were used to accurately measure the precise crack length. After removing the specimen from its substrate the cracks were virtually invisible even for an AFM [23]. Cracks normal to the edge of the specimen, were used for Mode-I fracture toughness measurements, which are easy to analyze, as linearly elastic fracture mechanics (LEFM) solutions are readily available.

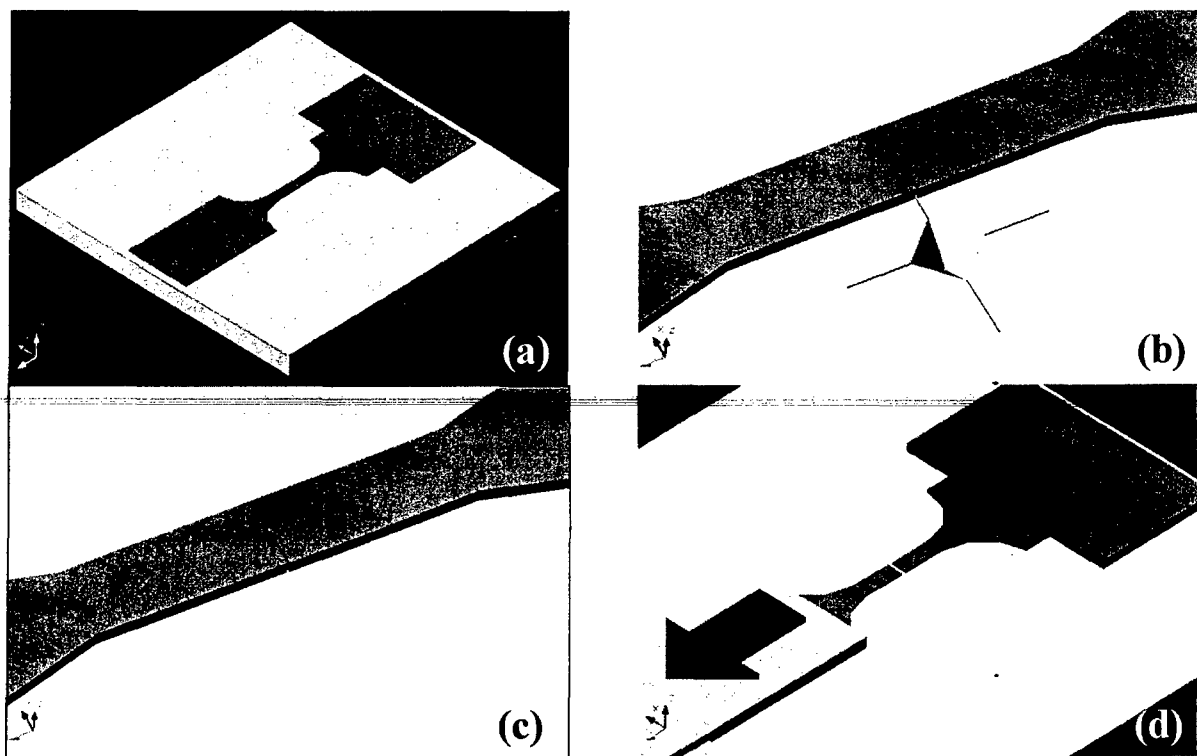


**Figure 11.** (a) Specimen before indentation, (b) Indentation of  $\text{SiO}_2$  adjacent to specimen gage section, (c) Freestanding specimen with edge pre-crack after substrate removal, (d) Fracture after crack propagation.

The cracks that were straight and perpendicular to the specimen gage axis were used to measure the material toughness. Figures 12 (a,b) show such a crack at two different scales, i.e. at the crack length and also near the crack tip pointing out to the proper geometry of these cracks for fracture studies.

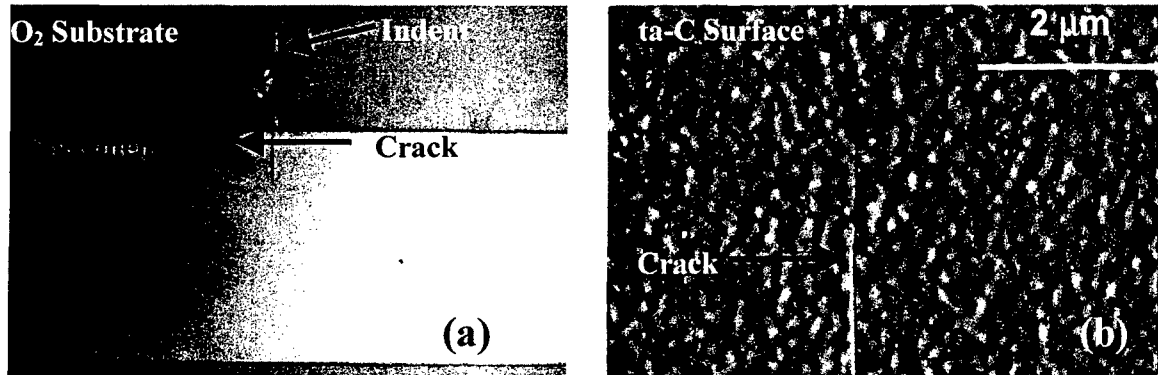


**Figure 12.** (a) Indentation on SiO<sub>2</sub> substrate and crack propagation in a 100-μm wide specimen, (b) AFM image of pre-cracked ta-C specimen before release from its substrate.

### Fracture toughness of polysilicon (YEARS 2 & 3)

The freestanding fracture specimens were tested *in situ* via the AFM/DIC method and measurements of local deformation fields in the vicinity of cracks in MEMS-scale specimens were obtained for the first time [18,23,24]. For each test the full-field displacements were recorded with 1-2 nm spatial displacement resolution. The analytical displacement solution in the vicinity of the edge crack was compared to the experimental displacement fields obtained via AFM/DIC at different increments of stress intensity, Figure 13. The measured  $K_{Ic, PolySi}$  was 15-20% higher than the minimum  $K_{Ic}$  for single crystal silicon [27]. This was the effect of polycrystallinity and anisotropy on the value of the macroscopic (apparent) fracture toughness as reported before in the context of microscopic [28] and macroscopic [29] numerical studies. Table II presents the  $K_{Ic, PolySi}$  and  $K_{Ic, ta-C}$  values for various specimen thicknesses and fabrication runs.

**Table II. Fracture toughness of MUMPs polysilicon and ta-C [18,23, 30]**

Material		Specimen Thickness (μm)	$K_{Ic}$ (MPa√m)	$K_{Ic}$ (MPa√m) (Average)
Polysilicon	MUMPs39	1.5	1.06±0.1	
	MUMPs39	2.0	1.05±0.2	1.00±0.1
	MUMPs41	2.0	0.98±0.1	
ta-C <sup>3</sup>		0.5	4.25±0.7	
		1.0	4.40±0.4	4.00±0.5
		2.2	3.40±0.4	
		3.0	3.06±0.17	

<sup>3</sup> Uncorrected for residual stresses



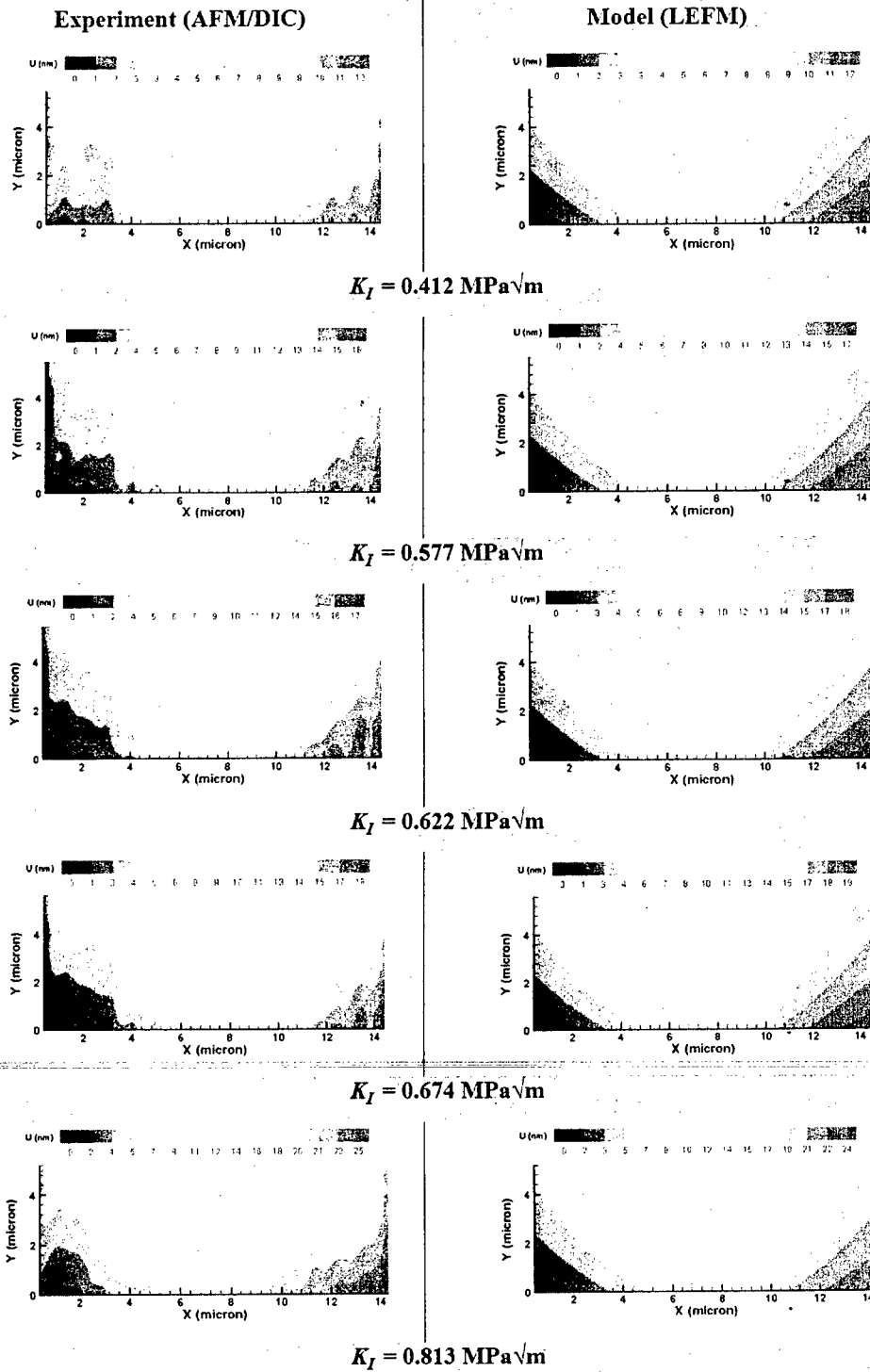


**Figure 13.** Axial displacements in the vicinity of a crack tip for increasing  $K_I$  (*Poly-Si*) as obtained by (left) AFM/DIC and (right) LEFM, respectively. The crack tip is located at the root of the contours. Images are best viewed in color.

The average fracture toughness of polysilicon between different fabrication runs and different structural layers of the MUMPs process was virtually the same. However, Figure 14 shows that crystal anisotropy in brittle polysilicon allows for incremental crack growth requiring a stochastic treatment of the macroscopic fracture toughness of polysilicon for MEMS. Significant grain randomness and anisotropy would require the fracture toughness be described in statistical terms. Using the AFM/DIC method, direct experimental evidence of incremental crack growth in (brittle) polysilicon was obtained for the first time via spatially resolved crack growth measurements [18,24]. In Figure 14 incremental crack growth between individual polysilicon grains was recorded at  $K_{I, PolySi} = 0.835 \text{ MPa}\sqrt{\text{m}}$  and  $K_{I, PolySi} = 0.896 \text{ MPa}\sqrt{\text{m}}$ . Small increments of the apparent stress intensity factor resulted in repeatable crack propagation and crack arrest. Further validation for these observations was provided by the corresponding crack tip displacement fields acquired at each crack increment. This incremental crack growth in brittle polycrystalline silicon was attributed to its polycrystalline structure and the associated variability in the local cleavage energy. Crack propagation was controlled by grains with varying orientations that resulted in variable cleavage energies along the crack path and thus crack arrest. A close-up in the fracture surface generated during sub-critical crack growth showed that the surface is mostly mirror with limited hackle [18].

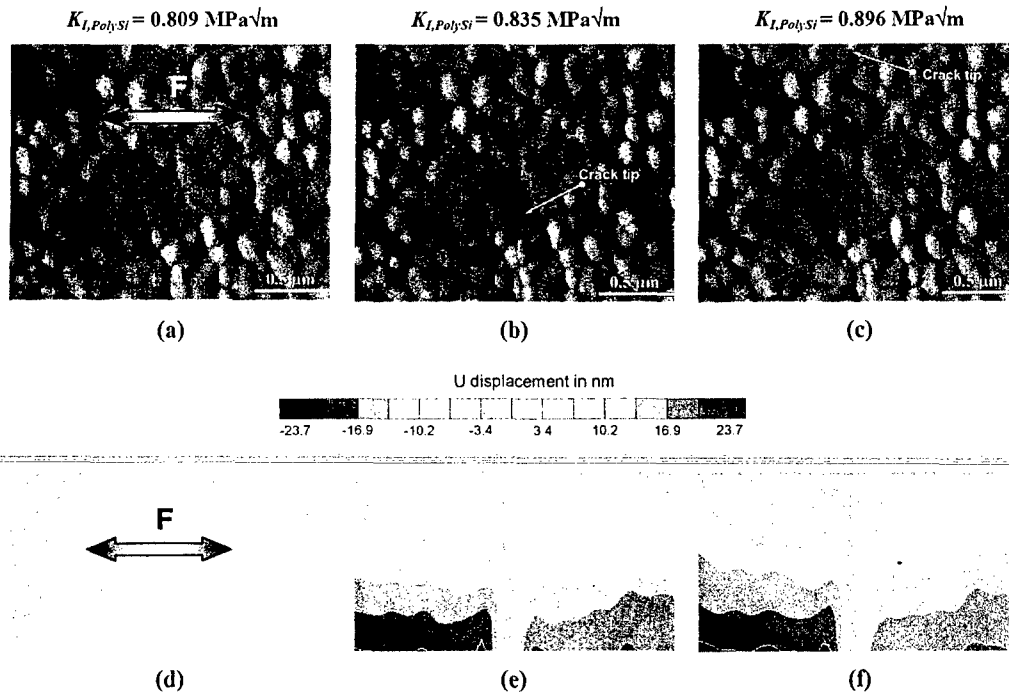


**Figure 14.** AFM micrographs of sub-critical crack growth in a freestanding polysilicon film with the corresponding local displacement fields. (a) The crack tip is below the field of view at the specimen centerline, (b) crack tip location after the first step of incremental crack growth, and (c) crack tip location after second crack growth. In (c) the crack is arrested at the grain boundary. After (c) the crack grew catastrophically at  $K_{I, PolySi} = 1.063 \text{ MPa}\sqrt{\text{m}}$ . The displacement contours (d-f) correspond to AFM images (a)-(c) respectively but span wider fields of view ( $10 \times 6 \mu\text{m}^2$ ) [18]. Images are best viewed in color.

### Fracture toughness of ta-C MEMS (YEARS 2 & 3)

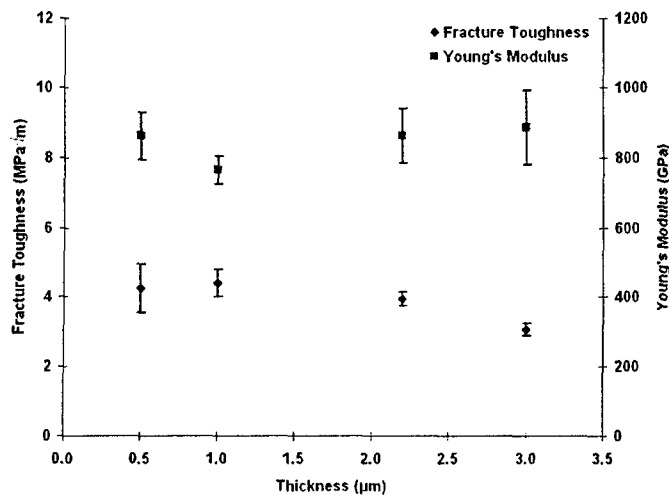


**Figure 15.** Elastic moduli and fracture toughness of ta-C films as a function of film thickness. The ta-C modulus was independent of thickness contrary to the fracture toughness [30].

films with different thickness [30]. The elastic modulus was independent of thickness, which implies that the dependence of ta-C fracture toughness on film thickness was not due to a variable modulus value. Instead, this dependence of fracture toughness on specimen thickness was attributed to specimen bending due to the residual stress gradient. When fracture tests were conducted, the axial loading compensated for the bending of the specimen and as a result mode I loading was generated by pure tensile loading and a bending moment. Thick films underwent extended annealing due to the fabrication method<sup>4</sup>, thus causing stress relaxation across the film thickness that was more pronounced compared to thinner films.

Finally, the validity of using U-notched Micro Compact Tension (MCT) specimens to calculate the fracture toughness of MEMS materials was investigated. ta-C specimens with deep U-type notches were microfabricated. An example of such a specimen is shown in Figure 16(a). The “fracture toughness” estimate from such notched specimens should be larger than that measured from samples with mathematically sharp cracks [23]. The stress,  $\sigma_\infty$ , required to cause failure due to a “blunt” crack (U-shaped notch) is higher than that required to cause failure due to a sharp crack for the same shape factor  $Y$  and slit/crack length  $a$ . From  $K_{Ic} = Y\sigma_\infty\sqrt{\pi a}$  it is inferred that the approximate fracture toughness calculated using a deep U-notch is higher than the  $K_{Ic}$  measured using a sharp crack. With this in mind MCT ta-C specimens with deep U-notches as seen in Figure 16 were tested and the data were analyzed as described in [23] to obtain  $K_{Ic} = 3.2 \pm 0.5$  MPa $\sqrt{m}$ . Although this estimate took into account the finite notch radius, fracture toughness tests of 1 μm thick ta-C specimens with atomically sharp cracks yielded  $K_{Ic} = 4.5 \pm 0.25$  MPa $\sqrt{m}$  which indicates that the use of deep U-notches along with the analysis based on a finite radius “crack” is not as accurate.

<sup>4</sup> Fabrication required deposition and annealing of many thin layers to avoid accumulation of compressive stress and film cracking.

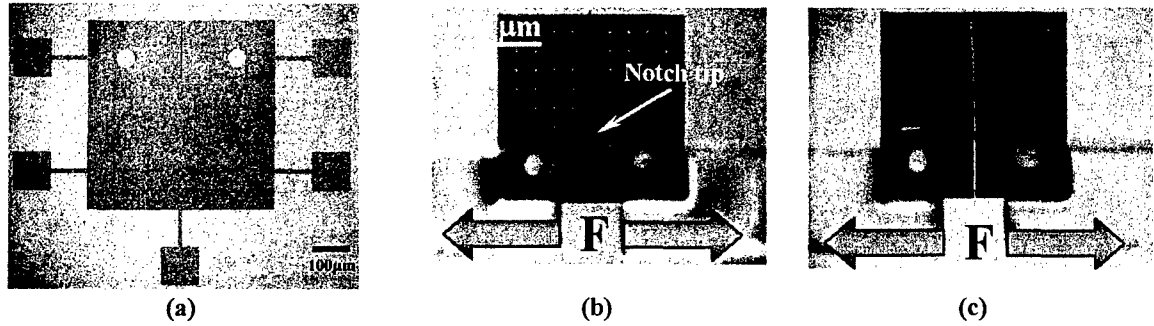


**Figure 16.** (a) Micro Compact Tension (MCT) specimen. The prefabricated U notch has 0.95 μm radius of curvature and 150 μm length. (b) ta-C MCT specimen loaded by glass grips. (c) MCT specimen after fracture; the crack propagated linearly from the notch root indicating good specimen alignment.

## V. Fracture due to Mixed Mode I/II Loading (YEAR 3)

Mixed mode I/II cracks were generated using the same method as in the study of mode I fracture. Figure 17 shows the fabrication and the details of an oblique edge pre-crack created with a Vickers microhardness tester.

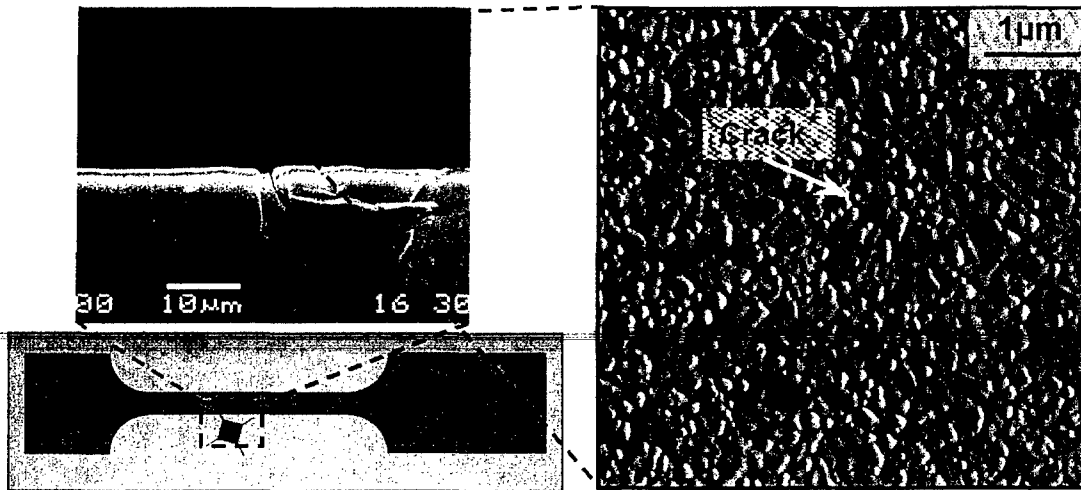


**Figure 17.** Schematic of indent created to produce an inclined edge pre-crack and detail of the inclined edge crack tip in polysilicon images with an AFM.

The mixed mode I/II stress intensity factors,  $K_I$  and  $K_{II}$ , are given by [31]

$$\begin{aligned} K_I &= Y_I \sigma_\infty \sqrt{\pi a} \cos^2(\beta) \\ K_{II} &= Y_{II} \sigma_\infty \sqrt{\pi a} \sin(\beta) \cos(\beta) \end{aligned} \quad (4)$$

where  $Y_I$  and  $Y_{II}$  are the mode I and mode II shape factors, and  $\beta$  is the inclined crack angle measured from the normal to the loading direction.

Due to specimen and loading geometry there were no close form solutions available to calculate  $K_I$  and  $K_{II}$  directly from boundary measurements. Instead, a finite element (FE) analysis was conducted to deduce the fracture parameters from the experimental data. Figure 18 shows the boundary conditions used in the FE analysis to extract  $K_I$  and  $K_{II}$ . The specimen length in the model was  $L = 5w$  and it was iteratively determined so that it would not bias the computed  $K_I$  and  $K_{II}$ . The deformation fields were derived using FRANC2DL [32] and the calculation of stress intensities was carried out by computing the J-Integral and the crack opening displacement. In the later case the  $K_I$  and  $K_{II}$  fracture toughness values were computed using the FE displacements as [32]

$$K_I = \frac{\mu\sqrt{2\pi}(V_{upper} - V_{lower})}{\sqrt{r}2(1-\nu)}$$

$$K_{II} = \frac{\mu\sqrt{2\pi}(U_{upper} - U_{lower})}{\sqrt{r}2(1-\nu)}$$
(5)

where,  $V$  and  $U$  are the crack opening displacements at a distance  $r$  from the crack tip in the mode-I and mode-II directions of the quarter point elements. In the J-integral evaluation, the area integral proposed by Li et al. [33] was used in conjunction with the mode separation technique developed by Ishikawa [34] and Bui [35].

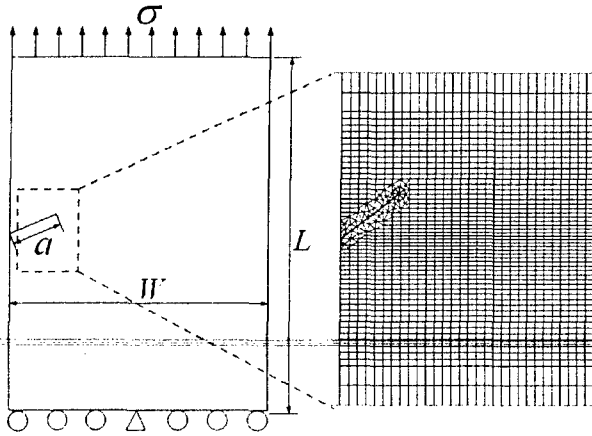


**Figure 18.** Specimen model and boundary conditions employed in the FE analysis to extract the mixed mode I/II stress intensity factors. The specimen length in this model was  $L = 5w$  [36].

The mixed-mode  $K_I$  and  $K_{II}$  parameters for polysilicon were obtained from experiments conducted on specimens with crack angles in the range  $\beta = 6^\circ$ - $55^\circ$ . The possible crack angles using this approach were limited because the Vickers micro-hardness indenter generates four cracks at  $90^\circ$  apart. Appropriate positioning of the indenter tip with respect to the specimen edge allowed for  $\beta_{max} = 55^\circ$ . After a short segment of crack initiation angle, the crack propagated, as expected, normally to the direction of the far field load. The normalized stress intensity factors,  $K_I/K_{Ic}$  and  $K_{II}/K_{Ic}$ , where  $K_{Ic} = K_{I, PolySi}$ , are plotted in Figure 19(a). The number next to each datum point is the pre-crack angle. Using the mixed mode I/II failure

criteria of maximum tensile (or hoop) stress (MTS) and maximum energy release rate (MERR) [31], the locus of  $K_I/K_{Ic}$  vs.  $K_{II}/K_{Ic}$  is plotted in the same figure with the solid and dashed lines, respectively. For both the MTS the MERR criterion,  $K_{Ic} = K_{I, PolySi}$  as measured in the mode I tests described in the previous section.

The MTS and MERR trajectories are valid for homogeneous and isotropic materials and are included in Figure 19(a) for comparison purposes with the experimental data. The

pronounced scatter of  $K_I$  at  $\beta < 20^\circ$  again indicates the stochastic nature of the effective  $K_{I, PolySi}$ . On the contrary, the  $K_{II}$  values were more sensitive to the pre-crack angle and were ordered accordingly. The trend of the experimental data agreed reasonably well with predictions by MTS the MERR criteria for  $\beta < 45^\circ$ . The geometry of the fracture specimens prepared for this work was subject to fabrication and mechanical testing constraints and it did not allow for comparisons with predictions by the MTS and MERR criteria [37] for  $\beta > 45^\circ$ . This deviation is clear for the datum point at  $\beta = 55^\circ$ . The decrease in  $K_{II}/K_{Ic}$  for  $\beta = 55^\circ$  is in agreement with literature reports of macroscopic tests where  $K_{II}/K_{Ic}$  was smaller for inclination angles larger than  $45^\circ$  [37].

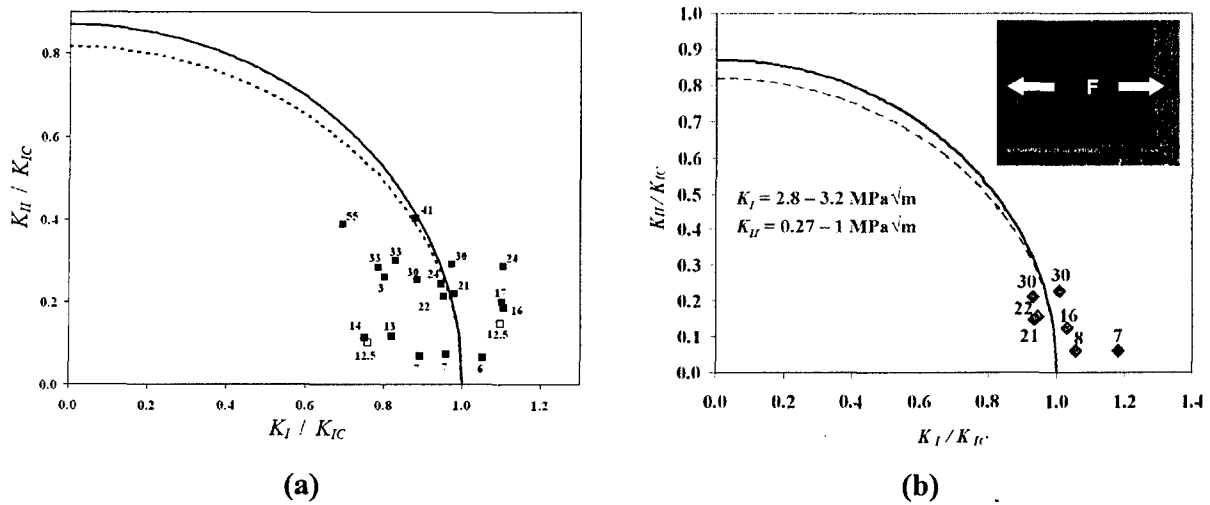


**Figure 19.** (a)  $K_I/K_{Ic}$  vs.  $K_{II}/K_{Ic}$  computed from inclined edge pre-cracks in polysilicon specimens. The experimental data are compared to predictions by MERR (dashed line) and MTS (solid line) criteria. The numbers next to data points are the pre-crack angles. The two open symbols correspond to the crack images in Figures 20(a,b) [36]. (b)  $K_I/K_{Ic}$  vs.  $K_{II}/K_{Ic}$  computed from inclined edge pre-cracks in ta-C specimens. The range of values is also shown [38].

An uncertainty analysis [36] showed that the deviation of the experimental data in Figure 19(a) from the two theoretical criteria was not due to experimental uncertainties that were quite small. Instead, the major reason was the random location for the crack tips inside individual grains or at triple junction points and grain boundaries. The two open symbols in Figure 19(a) point to significantly different  $K_I/K_{Ic}$  and  $K_{II}/K_{Ic}$  values for specimens with the same gage dimensions, crack lengths, and pre-crack angles. A close examination of the AFM images of the crack tip regions before the samples were released from their substrate showed that the crack tip in Figure 20(a) was located inside a large grain and fracture was initiated at considerably smaller  $K_I$  compared to the crack in Figure 20(b) whose tip was located at a triple junction point and resulted in large  $K_I$ . Thus, in both mode I and mixed mode I/II fracture, the grain boundaries and the triple junction points provided enhanced resistance to crack initiation (stochastic toughening) compared to the polysilicon grains. Then, the randomness in the generation of pre-cracks resulted in significant scatter in  $K_I$ , and  $K_{Ic, PolySi}$  and in limited extent in  $K_{II}$ .

The locus of  $K_I/K_{Ic}$  and  $K_{II}/K_{Ic}$  values for ta-C was very consistent with MERR (dashed line) and MTS (solid line) criteria as shown in Figure 19 (b). Ta-C is an amorphous material and at the

scale of this study it follows LEFM. Thus, its fracture is fully predicted by existing theories and experimental data may be extrapolated within the limits of LEFM. This provides an additional advantage of the use of ta-C instead of polysilicon in critical MEMS applications that are subject to overloads.

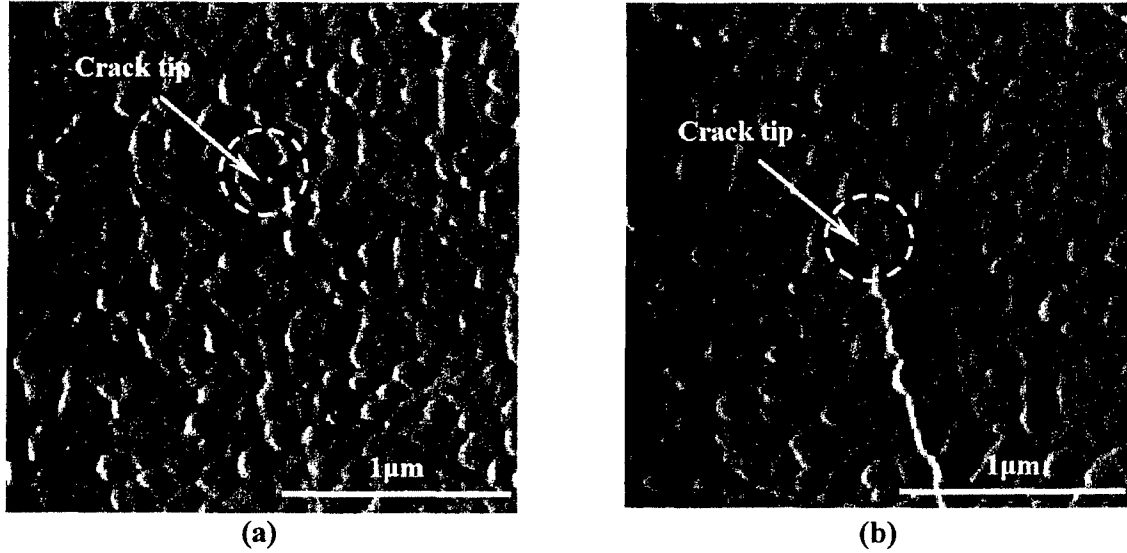


**Figure 20.** AFM images of two  $12.5^\circ$  pre-cracks whose  $K_I/K_{IC}$  vs.  $K_{II}/K_{IC}$  values in Figure 19(a) lie (a) to the left, and (b) to the right of the lines for the MERR and the MTS criteria. In (a) the crack tip resides in the large grain inside the circle, and in (b) the crack tip is located at a triple junction.

The analysis of mixed mode fracture was completed with the calculation of the theoretical crack initiation angles and their comparison with the experimental data. For instance, the crack initiation angle,  $\theta^*$ , for the specimen with  $\beta = 41.2^\circ$  in Figure 21(a) can be calculated as a function of the crack inclination angle,  $\beta$ , by [31]

$$\frac{K_{II}}{K_I} = \tan(\beta) = \frac{-\sin(\theta^*)}{3\cos(\theta^*) - 1} \quad (6)$$

For  $\beta = 41.2^\circ$  equation (6) gives  $\theta^* = 51^\circ$  whereas the measured crack initiation angle in the SEM micrograph in Figure 21(a) was  $48^\circ$ . While the difference in this example was small, other measured crack initiation angles deviated from the theoretical by  $5^\circ$  or more. The crack initiation angles are expected to be in general slightly different from the theoretically predicted because of small irregularities in specimen geometry and the angle crack plane with respect to the specimen cross-section, and in particular here because of cleavage anisotropy in polysilicon. In the case of polysilicon the deviation of crack initiation angle from the theoretical is associated with the grain anisotropy that did not allow for a smooth transition from the pre-crack angle to a path of straight crack propagation, Figure 21(a). On the other hand, in ta-C the transition from the pre-crack angle to a straight crack propagation path was very smooth, Figure 21(a), but the measured angles still deviated from the expected. It should be noted that such deviations were also observed in macroscopic mixed mode I/II fracture studies [39].

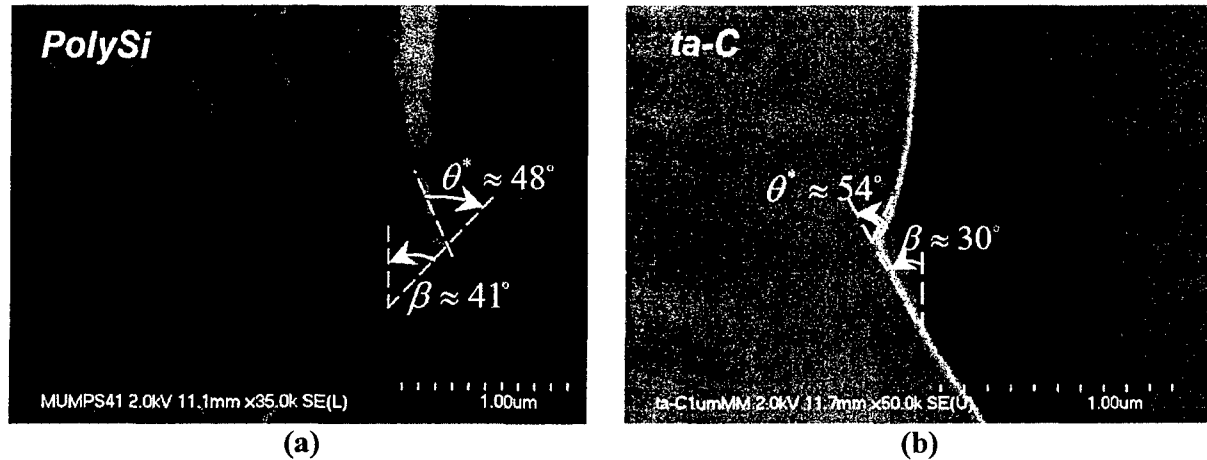


**Figure 21.** (a) Inclined edge pre-crack and crack initiation angle shown after fracture of a polysilicon specimen. The arrows show the direction of the applied far-field load. (b) SEM micrograph of pre-crack and crack initiation angle in a ta-C specimen [36,38].

### Conclusions on fracture studies of polysilicon MEMS

The mode-I fracture behavior of polycrystalline silicon was determined from MEMS-scale specimens and the average values of  $K_{Ic, PolySi}$  were in agreement with prior reports for nominally the same material fabricated by a different facility as well as for bulk polysilicon. The method followed in the present AFOSR project resulted in experimental uncertainties on the order of 1.5% owed to the use of an easy-to-calibrate external load-measurement device and accurate pre-crack length measurements. Compared to other methods for bulk and small-scale fracture tests the present method provided high accuracy in determining  $K_{Ic, PolySi}$  whose values were determined in the range of 0.843-1.225 MPa $\sqrt{m}$ . The significant scatter in  $K_{Ic, PolySi}$  was attributed to local anisotropy, enhanced grain boundary toughness, and, to a smaller degree, to crack tip shielding due to polycrystallinity [18]. The location of the crack tip (individual grain, or triple junction point) resulted in different local and macroscopic (apparent) stress intensity factors, which has also been predicted by literature models for brittle polycrystalline materials. Furthermore, this mechanism provided the basis to explain our direct observations of incremental (sub-critical) crack growth for  $K_{I, PolySi} < K_{Ic, PolySi}$ .

These local controlling mechanisms of fracture initiation were also present in the mixed mode I/II fracture [36,38]. The locus of  $K_I$  vs.  $K_{II}$  was determined for pre-crack inclination angles up to 55° and it demonstrated a scatter in  $K_I$  values similar to that for  $K_{Ic, PolySi}$ , which was shown to be the result of the location of the inclined crack tip. When the latter lied at a triple junction point the enhancement in  $K_I$  was as high as 50% compared to an inclined crack with its tip located inside a grain. For  $\beta \leq 41^\circ$  the values of  $K_{II}$  were very sensitive to the original crack angle while most of the values of  $K_I$  lied within the range of  $K_{Ic, PolySi}$  obtained in mode I fracture tests.



## VI. References

- [1] I. Chasiotis, W.G. Knauss, "A New Microtensile Tester for the Study of MEMS Materials with the aid of Atomic Force Microscopy", *Experimental Mechanics* **42** (1), pp. 51-57, (2002).
- [2] I. Chasiotis, Invited Paper: "Mechanics of Thin Films and Microdevices", *IEEE Transactions of Devices, Materials, and Reliability* **4** (2), pp. 176-188, (2004).
- [3] S.W. Cho and I. Chasiotis, "Elastic Properties and Representative Volume Element of Polycrystalline Silicon for MEMS," in press in *Experimental Mechanics* **47** (1), (2007).
- [4] D.A. Koester, R. Mahadevan, B. Hardy, K.W. Markus, "MUMPs Design Handbook," (2001).
- [5] J.J. Sniegowski, "Multi-level polysilicon surface-micromachining technology: applications and issues," International Mechanical Engineering Congress and Exposition, *Proceedings of the ASME Aerospace Division AD* **52**, pp. 751-759, (1996).
- [6] T.A. Friedmann, J.P. Sullivan, J.A. Knapp, D.R. Tallant, D.M. Follstaedt, D.L. Medlin and P.B. Mirkarimi Thick stress-free amorphous-tetrahedral carbon films with hardness near that of diamond *Appl. Phys. Lett.* **71** 3820-3822, (1997)
- [7] J.P. Sullivan, T.A. Friedmann, M.P. De Boer, D.A. La Van, R.J. Hohlfelder, C.I.H. Ashby, M.T. Dugger, M. Mitchell, R.G. Dunn, and A.J. Magerkurth Developing a new material for MEMS: Amorphous diamond, *Proceedings of the Materials Research Society*. **657** EE7.1, (2000)
- [8] I. Chasiotis, S. Cho, T.A. Friedman, and J. Sullivan, "Young's Modulus, Poisson's Ratio, and Nanoscale Deformation Fields of MEMS Materials", *Proceedings of the Materials Research Society* **795**, Boston, MA, pp. U.10.9.1- U.10.9.6, (2004).
- [9] I. Chasiotis, "Experimental Mechanics for MEMS and Thin Films: Direct and Local Sub-Micron Strain Measurements", in *Micromechanics and Nanoscale Effects: MEMS, Multi-Scale Materials and Micro-Flows*, Editors: V. M. Harik and L.-S. Luo, Kluwer Academic Press, pp. 3-37, (2004).
- [10] S.W. Cho, I. Chasiotis, T.A. Friedman, and J. Sullivan, "Direct Measurements of Young's Modulus, Poisson's Ratio and Failure Properties of ta-C MEMS", *Journal of Micromechanics and Microengineering* **25** (4), pp. 728-735, (2005).
- [11] B.D. Jensen, M.P. de Boer, N.D. Masters, F. Bitsie, and D.A. LaVan, "Interferometry of actuated microcantilevers to determine material properties and test structure nonidealities in MEMS," *Journal of Microelectromechanical Systems* **10** (3), pp. 336-346, (2001).
- [12] J.F. Cárdenas-García, S. Cho, and I. Chasiotis, "Thin Film Material Parameters Derived from Full Field Nanometric Displacement Measurements in Non-uniform MEMS Geometries", *Proceedings of Materials Research Society* **795**, Boston, MA, pp. U.11.28.1- U.11.28.6, (2004).
- [13] S. Cho, J.F. Cárdenas-García, and I. Chasiotis, "Measurement of Nano-displacements and Elastic Properties of MEMS via the Microscopic Hole Method", *Sensors and Actuators A Physical* **120**, pp. 163-171, (2005).
- [14] I. Chasiotis, W.G. Knauss, "Experimentation at the Micron- and Submicron Scale", in Comprehensive Structural Integrity Vol. **8**. Interfacial and Nanoscale Failure. Volume Editors: W. Gerberich and W. Yang, Elsevier Science, pp. 41-87, (2003).
- [15] R. L. Mullen, R. Ballarini, Y. Yin, and A.H. Heuer, "Monte Carlo Simulation of Effective Elastic Constants of Polycrystalline Thin Films," *Acta Materialia* **45** (6), pp. 2247-2255, (1997).
- [16] Z.Y. Ren, Q.S. Zheng, "A Quantitative Study of Minimum Sizes of Representative Volume Elements of Cubic Polycrystals - Numerical Experiments," *Journal of the Mechanics and Physics of Solids* **50**, pp. 881-893, (2002).
- [17] A.A. Elvin, "Number of Grains Required to Homogenize Elastic Properties of Polycrystalline Ice," *Mechanics of Materials* **22**, pp. 51-64, (1996).
- [18] I. Chasiotis, S.W. Cho, K. Jonnalagadda, "Fracture Toughness and Subcritical Crack Growth in Polycrystalline Silicon", *Journal of Applied Mechanics* **73** (5), pp. 714-722, (2006).

- [19] I. Chasiotis, W.G. Knauss, "The Mechanical Strength of Polysilicon Films: 2. Size Effects Associated with Elliptical and Circular Perforations", *Journal of the Mechanics and Physics of Solids* **51**, pp. 1551-1572, (2003).
- [20] Amanda McCarty, "Strength Size Effects in Polysilicon MEMS with Non-Uniform Geometries and Multiple Flaw Populations", *M.S. Dissertation*, University of Virginia, (2005).
- [21] A. McCarty and I. Chasiotis, "Description of Brittle Failure of Non-uniform MEMS Geometries", (to appear) *Thin Solid Films* (2006). (available online)
- [22] A. McCarty and I. Chasiotis, "Quantitative Failure Analysis for MEMS Materials with Multiple Active Flaw Populations," *Proceedings of the Society for Experimental Mechanics*, Portland, OR, June 5-7, (2005).
- [23] I. Chasiotis, S.W. Cho, K. Jonnalagadda, A. McCarty, "Fracture Toughness of Polycrystalline Silicon and Tetrahedral Amorphous Diamond-like Carbon (ta-C) MEMS," *Proceedings of the Society for Experimental Mechanics*, pp. 37-45, Costa Mesa, CA, June 7-10, (2004).
- [24] I. Chasiotis, S. Cho, K. Jonnalagadda, "Direct Measurements of Fracture Toughness and Crack Growth in Polysilicon MEMS", *Proceedings of the MRS* **854E**, pp. U.10.6.1- U.10.6.6, (2005).
- [25] K. Jonnalagadda, S. Cho, I. Chasiotis, T.A. Friedman, and J. Sullivan, "Mode-I Fracture Toughness of Tetrahedral Amorphous Diamond-like Carbon (ta-C) MEMS", *Proceedings of the Materials Research Society* **854E**, pp.U.9.7.1- U.9.7.6, (2005).
- [26] C. Keller, "Microfabricated high aspect ratio silicon flexures," *MEMS Precision Instruments*, El Cerrito, CA, 1998, pp. 185-202.
- [27] C.P. Chen, and M.H. Leipold, "Fracture Toughness of Silicon", *American Ceramics Society Bulletin* **59**, pp. 469-472, (1980).
- [28] R. Ballarini, R. L. Mullen, A.H. Heuer, *International Journal of Fracture* **95**, pp. 19-39, (1999).
- [29] K. Abdel-Tawab, G.J. Rodin, *International Journal of Fracture* **24**, pp. 1-13, (1998).
- [30] K. Jonnalagadda, S. Cho, I. Chasiotis, T.A. Friedman, J. Sullivan, "Film Thickness Effect on Fracture Toughness of Tetrahedral Amorphous Diamond-like Carbon", submitted to *Journal of the Mechanics and Physics of Solids*, (2005).
- [31] T.L. Anderson, "Fracture Mechanics", 2nd Edition, CRC Press, pp. 79-89, (1995).
- [32] A.R. Ingraffea, P.A. Wawrzynek, "Finite element methods for linear elastic fracture mechanics", *Comprehensive Structural Integrity*, R. de Borst and H. Mang (eds), Elsevier Science Ltd., Oxford, England, (2003).
- [33] F.Z. Li, C.F. Shih, and A. Needleman, "A comparison of methods for calculating energy release rates", *Engineering Fracture Mechanics* **21**, pp. 405-421, (1985).
- [34] H. Ishikawa, A finite element analysis of stress intensity factors for combined tensile and shear loading by only a virtual crack extension, *International Journal of Fracture* **16**, pp. 243-246, (1980).
- [35] H.D. Bui, "Associated path independent J-integral for separating mixed modes", *Journal of the Mechanics and Physics of Solids* **31**, pp. 439-448, (1983).
- [36] S.W. Cho K. Jonnalagadda, and I. Chasiotis, (Invited) "Mode I and Mixed Mode Fracture of Polysilicon for MEMS," to appear in *Fatigue and Fracture of Engineering Materials and Structures*, (2006).
- [37] P.S. Theocaris, G.A. Papadopoulos, "The influence of edge cracked plates on KI and KII components of the stress intensity factor studied by caustics", *J. Physics D: Applied Physics* **17**, pp. 2339-2349, (1984).
- [38] K. Jonnalagadda, and I. Chasiotis, "Mode I and Mixed Mode Fracture Toughness of Amorphous and Polycrystalline Materials for MEMS", in preparation for *International Journal of Fracture* (2007).
- [39] Professor K. Ravi-Chandar, U.T. Austin, personal discussions.